

Molecular ions in L1544. II. The ionization degree

P. Caselli , C. M. Walmsley,

and

A.Zucconi

Osservatorio Astrofisico di Arcetri, Largo E. Fermi 5, I-50125 Firenze, Italy;
caselli@arcetri.astro.it; walmsley@arcetri.astro.it; zucconi@arcetri.astro.it

M. Tafalla

Observatorio Astronómico Nacional (IGN), Campus Universitario, E-28800 Alcalá de Henares
(Madrid), Spain; tafalla@oan.es

L. Dore

Dip. Chimica "Ciamincian", Università di Bologna, Via Selmi 2, I-40126, Bologna, Italy;
dore@ciam.unibo.it

and

P. C. Myers

Harvard–Smithsonian Center for Astrophysics, MS 42, 60 Garden Street, Cambridge, MA 02138,
U.S.A.; pmyers@cfa.harvard.edu

ABSTRACT

The maps presented in Paper I are here used to infer the variation of the column densities of HCO^+ , DCO^+ , N_2H^+ , and N_2D^+ as a function of distance from the dust peak. These results are interpreted with the aid of a crude chemical model which predicts the abundances of these species as a function of radius in a spherically symmetric model with radial density distribution inferred from the observations of dust emission at millimeter wavelengths and dust absorption in the infrared. Our main observational finding is that the $N(\text{N}_2\text{D}^+)/N(\text{N}_2\text{H}^+)$ column density ratio is of order 0.2 towards the L1544 dust peak as compared to $N(\text{DCO}^+)/N(\text{HCO}^+) = 0.04$. We conclude that this result as well as the general finding that N_2H^+ and N_2D^+ correlate well with the dust is caused by CO being depleted to a much higher degree than molecular nitrogen in the high density core of L1544. Depletion also favors deuterium enhancement and thus N_2D^+ , which traces the dense and highly CO–depleted core nucleus, is much more enhanced than DCO^+ . Our models do not uniquely define the chemistry in the high density depleted nucleus of L1544 but they do suggest that the ionization degree is a few times 10^{-9} and that the ambipolar diffusion time scale is locally similar to the free fall time. It seems likely that the lower limit which one obtains to ionization degree by summing all observable molecular ions is not a

great underestimate of the true ionization degree. We predict that atomic oxygen is abundant in the dense core and, if so, H_3O^+ may be the main ion in the central highly depleted region of the core.

Subject headings: ISM: individual (L1544) – ISM: dust, extinction – ISM: molecules

1. Introduction

The ionization degree $x(e)$ ($= n(e)/n(\text{H}_2)$, with $n(e)$ and $n(\text{H}_2)$ the electron and H_2 number density, respectively) in dense molecular clouds plays a key role in determining the initial conditions which precede the collapse to form a star (e.g. Shu, Adams & Lizano 1987). If the magnetic field threading the dense gas is sufficiently large to prevent immediate collapse, ambipolar diffusion of neutrals across field lines can lead to a situation where a dense core of gas is gravitationally unstable. The time scale for such ambipolar diffusion is proportional to the ionization degree and it therefore becomes of interest to develop methods of estimating the ionization degree based upon the abundances of various species which trace the ionization in the dense gas.

In an earlier article (Caselli et al. 1998b, hereafter CWT98), we studied the possibility of using the $[\text{DCO}^+]/[\text{HCO}^+]$ abundance ratio as a tracer of the ionization degree in dense molecular gas, following previous work by Wootten, Snell & Glassgold 1979 and Guélin, Langer & Wilson 1982. We used the time-dependent models of Lee et al. 1996 to study the expected behavior of a variety of species thought to be relevant in this context and compared with the abundances measured by Butner et al. 1995. An analogous study carried out by Williams et al. 1998 reached very similar results. We confirmed earlier work (Dalgarno & Lepp 1984) which showed that a critical parameter in addition to the ionization degree which determines the fractionation of deuterated species (and hence abundance ratios such as $[\text{DCO}^+]/[\text{HCO}^+]$) is the degree of depletion of carbon and oxygen bearing species onto the surfaces of interstellar dust grains. Measuring the ionization degree in reliable fashion therefore requires the use of observations to solve for both $x(e)$ and depletion. One possible approach to this problem discussed by CWT98 was to use the cyanoacetylene (HC_3N) abundance as a “depletion indicator” (see also Ruffle et al. 1997). A more detailed analysis on the possibility to use HC_3N to estimate the degree of depletion in a dense core is currently under way (Comito et al., in prep.).

The CWT98 and Williams et al. 1998 studies used data with angular resolution of the order of an arc minute and did not search for spatial variations in the ionization degree and hence in the $[\text{DCO}^+]/[\text{HCO}^+]$ ratio. Studies of variations in the deuterium fractionation and in the degree of ionization across cores have been previously done in active star forming regions such as the R Coronae Australis molecular cloud (Anderson et al. 1999), and in massive cores located in regions that are currently forming stellar clusters (Bergin et al. 1999). In the former case, the electron fraction was found to decrease near the cluster of newly born stars, whereas in the latter

no differences in the ionization fraction were detected between cores with and without associated stars. No changes in the ionization fraction was found either between the edge and the center of the mapped regions. However, no similar studies have been performed so far in the direction of pre–star–forming cores in relatively quiescent zones of our Galaxy, which give the opportunity to investigate the initial conditions in the star formation process presumably not triggered by external agents.

In any model of a pre–protostellar cores, one expects to observe a concentration of material around the region of highest density. As the density becomes higher, one expects the degree of ionization to decrease, the degree of depletion onto dust grain surfaces to increase, and, consequently, the fractionation of deuterated species to be enhanced (e.g. Roberts & Millar 2000). In fact, one might naively expect that deuterated species correlated with high depletion might trace the phase prior to the formation of a protostar. With this in mind, we undertook observations using the IRAM 30-m telescope of a variety of species towards the dense core L1544 in the Taurus molecular cloud which is thought (e.g. Tafalla et al. 1998, Ciolek and Basu 2000) to be in a phase shortly prior to that at which collapse occurs. The data and a kinematical study of this region are presented in Caselli et al. (2001, hereafter Paper I). Here we present our determination of the electron fraction across L1544 and show that $x(e)$ at the center of the core – where the H_2 number density is $\sim 10^6 \text{ cm}^{-3}$ – is about 2×10^{-9} , about five times smaller than expected if the electron fraction is due to cosmic–ray ionization alone and the cosmic–ray ionization rate ζ has its “standard” value ($x(e) = 1.3 \times 10^{-5} n(H_2)^{-0.5}$; cf. McKee 1989).

In section 2, we show our determination of physical and chemical parameters of importance for electron fraction estimates. The determination of electron fraction is presented in Section 3. Finally in Section 4, we discuss the consequences of our measurements for the understanding of high density cores like L1544.

2. Determination of physical and chemical parameters

An accurate estimate of electron fraction implies measurements of (i) the column density of the observed molecular ions, (ii) the temperature as well as (iii) the density structure of the core, and (iv) the amount of CO depletion. In the following sections we will describe the above points separately.

2.1. The temperature across the core

Because of its low dipole moment, CO is likely thermalized at the typical core densities and it can be used to measure kinetic temperatures. Tafalla et al. 1998 used the $J = 1 \rightarrow 0$ transition of ^{12}CO , ^{13}CO and C^{18}O to determine the excitation temperature of the CO emitting gas across L1544 and found $T_{\text{ex}} \sim 12 \text{ K}$, in good agreement with previous kinetic temperature estimates

based on CO and NH₃ observations (~ 10 K; Myers et al. 1983, Ungerechts et al. 1982, Benson & Myers 1989). We repeated a similar analysis using C¹⁸O(1–0) and C¹⁷O(1–0) data and found an average value of $T_{\text{ex}} = 10.1 \pm 0.1$ K. Of course, CO is not a good tracer of gas temperature at densities $\gtrsim 10^5 \text{ cm}^{-3}$, where it is strongly depleted (CWT99; see Sect. 2.3). A recent Monte Carlo radiative transfer analysis of the two inversion transitions of NH₃, observed at the Effelsberg antenna (Tafalla et al., in prep.; 40'' half power beamwidth), has also shown that $T_{\text{k}} \sim 10$ K with no significant variation across L1544. We assume on this basis a constant temperature of 10 K in the rest of our analysis. However, model calculations of the dust temperature in pre-stellar cores (Zucconi et al. 2001, Evans et al. 2001) predict a fall off in dust temperature from ~ 14 K at the edge to ~ 7 K at the center. This is likely to be reflected also in the behaviour of the gas temperature at least for densities above 10^5 cm^{-3} . Although for our purposes we can neglect such findings (our simple chemical model presented in Sect. 3.2 is not significantly affected by a change in temperature from 10 to 7 K), the predicted temperature gradient affects our estimates of the volume density from N₂H⁺, as discussed below.

2.2. The density across the core

From our molecular line data we can deduce good number density estimates only at the L1544 “molecular peak” and in a few adjacent positions (see Sect. 2.2.1, 2.2.2). Therefore, for our electron fraction estimates across L1544 (Sect. 3.2) we used the density profiles obtained from 1.3mm continuum observations (Ward–Thompson et al. 1999, hereafter WMA) and ISOCAM absorption in the mid-infrared (Bacmann et al. 2000, hereafter BAP). These density profiles are described in Section 3.2.1.

A number of line intensity ratios measured by us are sensitive to density. Since the line ratios depend on collisional rates, one in principle derives $n(\text{H}_2)$ independently of assumptions about abundance. However, in a situation where the density varies rapidly along the line of sight (as suggested by the dust emission and absorption), the density which one derives will be a weighted mean. In the following, we describe some estimates we have made using different tracers.

2.2.1. Density inferred from DCO⁺(3–2)/DCO⁺(2–1)

Our observations of DCO⁺(3–2) and (2–1) allow estimates to be made of the hydrogen number density in the regions responsible for the emission of these lines as well as estimates of the DCO⁺ column density. We have done this using an LVG statistical equilibrium code similar to that described e.g. in Walmsley (1987). The approach is essentially identical to that discussed by Butner et al. 1995. The collisional rates were taken from those calculated for collisions of para-H₂ with HCO⁺ by Monteiro (1985) assuming a temperature of 10 K. At this temperature, the rates are essentially identical to the more recent rates of Flower 1999. We assumed a dipole moment of

3.9 Debye following Botschwina 1989 (see also Williams et al. 1998).

In Fig. 1, we show the results obtained in this manner superimposed upon the half-maximum contours of the $\text{DCO}^+(2-1)$ and $(3-2)$ maps (see Paper I for details on these data) and the 1.3mm continuum map of WMA. We see a definite tendency for the highest densities derived from DCO^+ to be close to the dust emission maximum. We see also that the values found for $n(\text{H}_2)$ towards the dust peak are close to those derived by WMA from their observations ($\sim 10^6 \text{ cm}^{-3}$). However, there are a number of *caveats* of which one should be aware.

One of these is that the $\text{DCO}^+(2-1)$ line is almost certainly optically thick towards the core of L1544. This is suggested by both our LVG results themselves and the comparison at offset (20,-20) with D^{13}CO^+ (see Paper I) which suggests an optical depth of order 4. Our density estimates are thus sensitive to the geometry and velocity gradients within L1544. We note additionally that our $\text{DCO}^+(3-2)$ map cannot be convolved to the 2–1 resolution (1.5 times worse) because it is undersampled (grid of 1.7 times HPBW). Nevertheless, our results suggest that we are sampling in DCO^+ the high density inner core of L1544.

2.2.2. Density derived from N_2H^+ and N_2D^+

Our N_2H^+ and N_2D^+ observations allow an independent estimate of the density. This is of special interest because, as we have seen in Paper I, the N_2H^+ and, in particular, the N_2D^+ integrated intensity maps appear to trace best the dust emission (see also Bergin et al. 2001). Another characteristic of these species is that, due to the hyperfine splitting, we can determine directly the optical depth in several transitions utilising the relative intensities of the hyperfine satellites. This reduces considerably the errors in our determinations of level column densities for, say, N_2H^+ , as compared to DCO^+ . Finally, it is of some importance that we have detected $\text{N}_2\text{H}^+(3-2)$ and $\text{N}_2\text{D}^+(3-2)$. This is because we expect such transitions to be essentially collision dominated in the sense that the integrated line intensity has, for a given temperature, a one-to-one correspondence with the integral of the product of the H_2 density and the N_2H^+ density along the line of sight. We call this integral $\int n(\text{H}_2)n(\text{N}_2\text{H}^+)ds$ the N_2H^+ collision measure $CM(\text{N}_2\text{H}^+)$ in the following. Essentially, the $(3-2)$ line intensities are proportional to $CM(\text{N}_2\text{H}^+)$ in the limit where collisional deexcitation is negligible with respect to radiative transitions which for $\text{N}_2\text{H}^+(3-2)$ at 10 K for example implies $n(\text{H}_2)$ less than 10^6 cm^{-3} .

We have developed an LVG code for $\text{N}_2\text{H}^+(\text{N}_2\text{D}^+)$ analogous to that for DCO^+ . We use the collisional rates of Green(1975) for collisions of N_2H^+ with He and multiply them by 1.4 to take account of the differing mass of H_2 . We also have adjusted the escape probability to account for hyperfine splitting in the 1-0, 2-1, and 3-2 transitions of N_2H^+ . We first use our determination of the optical depth in the $\text{N}_2\text{H}^+(1-0)$ line at offset (20, -20) to obtain an estimate of the N_2H^+ column density and find $N(\text{N}_2\text{H}^+) = 1.5 \cdot 10^{13} \text{ cm}^{-2}$ at offset (20, -20). Then, we determine $CM(\text{N}_2\text{H}^+)$ from $\text{N}_2\text{H}^+(3-2)$ data, which have been averaged in a 3×3 grid of positions spaced

by $10''$ and centered at (20, -20) (see Tab. 3 of Paper I, second row) in order to simulate a $20''$ beam, similar to the 1–0 observations. From the $CM(N_2H^+)/N(N_2H^+)$ ratio we find a mean density of $1.3 \times 10^5 \text{ cm}^{-3}$, smaller than the value derived above from our DCO^+ measurements and also smaller than the central densities suggested by the results of WMA and of BAP. These discrepancies may be partly due to the assumption of a constant temperature of 10 K, in particular in the dense highly CO–depleted nucleus of L1544, best traced by N–bearing molecules, where Zucconi et al. 2001 derive $T \sim 7 \text{ K}$.

We can in analogous fashion use our N_2D^+ observations to obtain a density estimate. At the center of L1544 assuming a temperature of 10 K, we find a mean density $CM(N_2D^+)/N(N_2D^+) = 1.5 \cdot 10^{18} / 4.9 \cdot 10^{12} = 3 \cdot 10^5 \text{ cm}^{-3}$. This is a factor of 2 higher than the N_2H^+ estimate above which might perhaps reflect the fact that the N_2D^+ emission is more compact than that of N_2H^+ . However, it is still a factor of 3 smaller than the density deduced from dust continuum and DCO^+ observations, again suggesting a possible temperature fall off in the core center.

2.3. Depletion of CO

The depletion factor f_D is defined by the ratio between the “canonical” fractional abundance of CO (9.5×10^{-5} , Frerking et al. 1982¹) and the observed $x(\text{CO}) = N(\text{CO})/N(\text{H}_2)$. To determine f_D at the dust peak position, CWT99 compared the $C^{17}\text{O}$ integrated intensity with the 1.3mm continuum dust emission flux density from WMA. They found that $f_D \sim 10$ at the dust peak, and that observations are consistent with a model where CO is condensed out onto dust grains at densities $\sim 10^5 \text{ cm}^{-3}$. The corresponding radius of the region where CO is severely depleted is $\sim 6500 \text{ AU}$ and the depletion causes $2.3 M_\odot$ of gas to be lost to view in molecular line emission.

Here we extend this analysis to all the other positions where $C^{17}\text{O}$ has been observed. To do this we divided the 1.3mm map by the $C^{17}\text{O}(1-0)$ map. This division implies three steps: (i) convolve the 1.3mm map with a $22''$ beam (the HPBW of the $C^{17}\text{O}$ observations) and reproject it to have the same coordinates as the $C^{17}\text{O}$ map; (ii) make a regularly sampled $C^{17}\text{O}$ map; (iii) divide one map by the other. The result of this operation can be translated into a depletion factor map. We somewhat arbitrarily assume “normalcy” to be given by $[C^{17}\text{O}]/[H_2] = 4.8 \times 10^{-8}$ (Frerking et al. 1982). Assuming an excitation temperature for $C^{17}\text{O}$ of 10 K and a 1.3 mm dust grain opacity $\kappa_\nu = 0.005 \text{ cm}^2 \text{ g}^{-1}$ (WMA), we find that the depletion factor f_D can be expressed as:

$$f_D = 0.027 \frac{S(1.3\text{mm, mJy}/22'')}{W_{C^{17}\text{O}}(\text{K km s}^{-1})}. \quad (1)$$

¹We note that the only direct measurements of the CO abundance give larger values than those reported by Frerking et al. 1982 by a factor of about 5 (Lacy et al. 1994), implying larger depletion factors than found in this work.

Here, $W_{\text{C}^{17}\text{O}}$ is the integrated intensity (over all hyperfine components) of $\text{C}^{17}\text{O}(1-0)$ and $S(1.3\text{mm}, \text{mJy}/22'')$ is the flux density at 1.3mm in a $22''$ beam. In those positions where only C^{18}O was observed, we used $f_{\text{D}} = 0.085 S(1.3\text{mm}, \text{mJy}/22'')/W_{\text{C}^{18}\text{O}}(\text{K km s}^{-1})$.

In Fig. 2 the depletion factor map is shown together with the 1.3mm continuum map from WMA. There is a fairly good correspondence between the f_{D} and 1.3mm contours as one might expect given the “flat” nature of the C^{17}O and C^{18}O maps. We note however that the peaks are not coincident and there is a projected distance between the f_{D} and the dust peaks is $13''$ (about half a beam). This appears significant but one must remember that the C^{18}O and C^{17}O maps are probably dominated by emission from gas of density a few times 10^4 cm^{-3} to the foreground or background of the dust emission core. Thus structures unrelated to the pre-protostellar core may influence our maps.

2.4. Molecular ion column densities

The methods used to estimate column densities of the observed species, which give same results within a factor of 2, are reported in appendix A. Here we show the results.

2.4.1. DCO^+ and HCO^+

The statistical equilibrium calculations used to estimate the H_2 density (see Sect. 2.2) can also be applied to a determination of the column densities of DCO^+ and HCO^+ . As in the case of density determination, our errors grow rapidly if the observed lines are optically thick. Towards the peak of L1544, we have used the optically thin species HC^{18}O^+ and D^{13}CO^+ to determine HCO^+ and DCO^+ column densities and C^{17}O to determine the CO column density. We have considerable confidence that in these three cases, the observed lines are in fact optically thin (see discussion in Sect. A.1). For C^{17}O , we can check (see e.g. CWT99) optical depth using the relative intensities of the hyperfine satellites.

We nevertheless for most of the following discussion use H^{13}CO^+ and DCO^+ column densities derived from transitions which are optically thick towards the dust emission peak and in the immediate vicinity. The reason for this is the greater extent of our maps in these lines. The justification is that our checks with the optically thin variants yield results which are consistent with those presented here. Thus we have checked our H^{13}CO^+ column densities using HC^{18}O^+ where available and our DCO^+ column density using the D^{13}CO^+ measurement at (20,-20). We conclude that our column density estimates are accurate to within a factor of 2 also when the optical depth is high (see appendix A.1 for details).

Bearing this in mind, we present in Fig. 3 our DCO^+ and HCO^+ column density maps. One sees in the first place that these differ considerably from the integrated intensity maps. While

for the reasons discussed above, the column density maps (or ratio maps) should be treated with caution, we consider them a better estimate than simply scaling the integrated intensity maps. We also show in Fig. 3 the inferred ratio of column densities $N(\text{DCO}^+)/N(\text{HCO}^+)$. DCO^+ is clearly more concentrated towards the structure seen in dust emission by WMA than is H^{13}CO^+ . Considering the column density ratio map, we see that $[\text{DCO}^+]/[\text{HCO}^+]$ appears to vary by almost an order of magnitude between the centre and the edge of the map (roughly an arc minute or 0.04 parsec). Away from the peak, the inferred $N(\text{DCO}^+)/N(\text{HCO}^+)$ ratios are considerably lower than found in the survey of Butner et al. 1995. This is somewhat surprising because we expect to be observing higher density gas on average with greater degrees of depletion than in the arc minute resolution Butner et al. 1995 survey. The Butner et al. 1995 estimates for $N(\text{DCO}^+)/N(\text{HCO}^+)$ vary between 0.02 and 0.07 whereas our results for L1544 vary from 0.04 near the dust peak to values a factor of 10 lower at the edge of our map.

2.4.2. N_2D^+ and N_2H^+

The N_2D^+ and N_2H^+ column density maps, together with $N(\text{N}_2\text{D}^+)/N(\text{N}_2\text{H}^+)$, are also shown in Fig. 3. Our N_2D^+ observations as noted previously (see also Paper I) show that N_2D^+ traces the dust peak emission better than any other species. It also turns out that the values we infer for $N(\text{N}_2\text{D}^+)/N(\text{N}_2\text{H}^+)$ are much higher than for $N(\text{DCO}^+)/N(\text{HCO}^+)$. At offset (20,-20), we infer $N(\text{N}_2\text{D}^+)/N(\text{N}_2\text{H}^+)=0.24\pm 0.02$. This is a factor of 4 higher than our maximum value for $N(\text{DCO}^+)/N(\text{HCO}^+)$. We conclude from this that the degree of deuterium enhancement increases towards the dust emission peak of L1544.

3. The electron fraction $x(e)$

CWT98 used a simple chemical model to find analytic expressions which allow one to directly estimate $x(e)$ (and the cosmic ray ionization rate ζ) once $N(\text{DCO}^+)/N(\text{HCO}^+)$, f_{D} , and $n(\text{H}_2)$ are known from observations (see their eqns. 3 and 4). However, these expressions furnish upper limits of $x(e)$ and ζ (see Section 3.1). In fact, in the simple chemical scheme used to derive CWT98 analytic expressions, dissociative recombination of molecular ions onto negatively charged dust grains and gaseous reactions involving atomic deuterium (see e.g. Dalgarno & Lepp 1984) are not taken into account. Moreover, this chemical model is only valid for homogeneous clouds, whereas L1544 clearly has a density structure and a varying amount of depletion and molecular abundances along the line of sight (see Sect. 2.4). In fact, CWT98 eqns.(3) and (4) have been applied to data with a significantly lower (factor of ~ 6) spatial resolution compared to the present observations, so that any gradient was smoothed out in the beam and resultant $N(\text{DCO}^+)/N(\text{HCO}^+)$, f_{D} , and $n(\text{H}_2)$ should be considered as “average” quantities for the cores. The same problem is met if “pseudo-time dependent” chemical codes are used. The density structure as well as differential depletion of molecular species has to be taken into account to reach a satisfactory agreement with

observations (see also Aikawa et al. 2001).

In this section, we discuss what one can say about the ionization fraction in L1544. One may obtain a lower limit to the ionization fraction $x(e)$ summing the abundances of observed molecular ions in L1544. This limit may be close to the real ionization fraction, if refractory metals of low ionization potential such as Mg and Fe are significantly depleted (see e.g. Fig. 2 of Caselli et al. 1998b).

We first briefly discuss the limits one can place on ionization degree based upon the observed molecular ion column densities.

3.1. Lower limits for $x(e)$

Lower limits of the electron fraction across L1544 can be obtained by simply summing up column densities of the observed molecular ions:

$$x(e)_l \geq \frac{N(\text{HCO}^+) + N(\text{DCO}^+) + N(\text{N}_2\text{H}^+) + N(\text{N}_2\text{D}^+)}{N(\text{H}_2)} \sim \frac{N(\text{HCO}^+)}{N(\text{H}_2)}. \quad (2)$$

$x(e)_l$ has been obtained for each observed position toward L1544 based upon the column density determinations from Sect. 2.4 and the column densities of WMA. We find in this way a lower limit at essentially all positions where H^{13}CO^+ was observed of : $\langle x(e)_l \rangle \sim 1 \times 10^{-9}$ with little variation.

These estimates do not however really sample the high density nucleus of L1544 and in order to do that, we use the model discussed in the following section.

3.2. $x(e)$ from chemical models

Deriving the behavior of the electron fraction as a function of radius is complicated however by the strong abundance gradients due to depletion. These cause observed quantities such as e.g. the HCO^+ column density to be strongly influenced by background and foreground emission in the observed lines. This is the main rationale for the simple model introduced below.

3.2.1. Model description

The results of WMA and BAP show rather clearly that the L1544 “core” itself contains a high density “core” where the density reaches values as large as $5 \cdot 10^5 \text{ cm}^{-3}$ over a volume of radius several thousand AU. We have shown previously (CWT99) that CO is depleted by at least an order of magnitude in the central high density peak. In this section, we consider the behavior of

the ions and of the electron density in the depleted region. We have done this with an extension of the model briefly described by CWT99 and used to fit the CO depletion.

We assume for this purpose a spherically symmetric density distribution with a constant molecular hydrogen density of (i) $5.4 \times 10^5 \text{ cm}^{-3}$ out to a radius $r_{\text{flat}} = 2900 \text{ AU}$ followed by a $1/r^2$ fall off out to a cut-off radius of 10000 AU, which simulates the results of BAP based on the extinction measured with ISOCAM against the emission of small particles at a wavelength of $7 \mu\text{m}$; (ii) $1.3 \times 10^6 \text{ cm}^{-3}$ out to a radius $r_{\text{flat}} = 2500 \text{ AU}$ followed by a $1/r^2$ fall off out to a cut-off radius of 13000 AU, as found by WMA on the basis of 1.3mm observations of dust emission. The H_2 column and volume density inside r_{flat} determined by BAP are a factor of 3.8 and 2.4, respectively, lower than those found by WMA (see however the comments in Table 2 of BAP). It is clear that this approximation is somewhat crude and indeed that the distribution departs considerably from spherical symmetry. Moreover, the recent study of Evans et al. 2001 has shown that the temperature drop in the L1544 core nucleus to about 7 K (in agreement with Zucconi et al. 2001) implies a steeper density profile than in the isothermal case of WMA and BAP. However, we believe that our simple model suffices to explain many of the observations.

As in CWT99, we have followed the time-dependent depletion of CO neglecting dynamic effects. That is to say, we assume the depletion time-scale to be more rapid than dynamical time-scales and assume initially a “canonical” CO abundance of 9.5×10^{-5} relative to H_2 . However, we also consider in this study the recycling of CO back into the gas-phase using the cosmic ray desorption rate proposed by Hasegawa & Herbst 1993 and a CO adsorption energy $E_D(\text{CO})$ to the grain surface of 1210 K (Hasegawa et al. 1992). This is for a surface of SiO_2 while for binding with a CO mantle, Sandford and Allamandola (1990) find $E_D(\text{CO})$ to be 960 K. This is critical for the model because we have, following Hasegawa & Herbst 1993, assumed a time-scale for cosmic ray desorption t_{cr} of species X given by :

$$1/t_{cr}(X) = 3 \cdot 10^{-7} \zeta_{17} \times \exp[-E_D(X)/70] \quad (3)$$

Here, ζ_{17} is the cosmic ray ionization rate in units of 10^{-17} s^{-1} and $E_D(X)$ is the adsorption energy in K of species X . Rough estimates suggest that “chemical” desorption due to molecular hydrogen formation (Willacy & Millar 1998) appears to be less effective. Indeed, a recent theoretical work by Takahashi & Williams 2000 has shown that the chemical desorption of CO can occur on small grains with size less than 20 \AA , but it is negligible on larger grains. A crucial point in our discussion moreover is that we also consider the analogous depletion of molecular nitrogen assuming an initial N_2 fraction of 7.5×10^{-5} (Meyer et al. 1997). This is a maximal value in that it is based on nitrogen depletion measurements in diffuse clouds. Critical for our model is also that we adopt a N_2 adsorption energy of $\leq 787 \text{ K}$ ($= 0.65 \times E_D(\text{CO})$; Bergin & Langer 1997 based upon calculations of Sadlej et al. 1995) considerably lower than that for CO. The exponential dependence of the cosmic ray desorption rate above causes more effective depletion of CO and gives rise to a layer where N_2 is the most abundant gas phase species containing heavy elements and where N_2H^+ is an abundant ion.

In a model of this type, one can write for the abundance $n(X)$ of species X (where X can be CO or N₂) relative to H₂ that :

$$n(X) = n(X, \infty) + (n_{tot}(X) - n(X, \infty)) \exp -(t/t_0). \quad (4)$$

Here, $n_{tot}(X)$ is the total abundance of X in both gas and solid phase , $n(X, \infty)$ is the steady state gas phase abundance given by $n_{tot}(X)/(1 + t_{cr}/t_{dep})$ and t_{dep} is the depletion time scale $1/(S n_{gr} \sigma_{gr} v(X))$ (where S is the sticking coefficient, n_{gr} is the grain number density, $v(X)$ is the thermal velocity of X , and σ_{gr} is the grain cross section). The time-scale t_0 is simply $(t_{dep} t_{cr})/(t_{dep} + t_{cr})$. We are assuming here that one can neglect destruction of X due to either gas or solid-phase reactions.

This rather crude model of depletion has the advantage that it can be rapidly computed as a function of density and time. For the present purpose, we (as in CWT99) continue the calculation until such time as we reach a central CO column density compatible with the observed C¹⁷O column density toward the central dust peak in L1544. At this point, as discussed by CWT99, the main contributions to the observed CO column come from lower density foreground and background material while CO in the central high density peak is depleted to very low abundances. The present calculations confirm this. Even though cosmic ray desorption is included, the central CO abundance is still depleted by a factor of 10^3 (~ 30), if the WMA (BAP) density structure is used. This also depends sensitively on $E_D(\text{CO})$ and indeed our results suggest that $E_D(\text{CO})$ must be larger than ~ 900 K in order to have depletion in the central region as observed (for the standard values of ζ and S , see Tab. 2). A similar result has also been found by Aikawa et al. 2001, who cannot reproduce the observed “hole structure” in the CO column density if the grain surface is covered by non-polar ice (i.e. $E_D(\text{CO}) = 960$ K).

Although the gas phase chemistry in general has long time scales, the ion chemistry is relatively rapid and thus one can expect in reasonable approximation that the abundances of ionic species such as HCO⁺, N₂H⁺ etc. are given by the steady state chemical equations using the instantaneous abundances of the neutral species which are important heavy element repositories. The time scale for the “ion chemistry” is expected to be determined by recombination to species such as HCO⁺ with a rate of $\beta_{diss} n(e)$ where β_{diss} is the dissociative recombination rate and $n(e)$ the electron density. For “canonical estimates” $n(e) \sim 10^{-3} \text{ cm}^{-3}$ and $\beta_{diss} \sim 10^{-6} \text{ cm}^3 \text{ s}^{-1}$, we find a time scale of 30 years for the ion chemistry which is much less than depletion time scales. Thus one can compute HCO⁺ in terms of the instantaneous CO abundance and N₂H⁺ in terms of the instantaneous N₂ abundance.

Analogously, the electron fraction $x(e)$ can be computed in terms of global estimates for the molecular and metallic ions and using the same instantaneous abundances for CO, N₂ etc. in the gas phase. The approach we have adopted is a simplified version of the reaction scheme of Umebayashi & Nakano 1990. Thus, we compute a generic abundance of molecular ions “mH⁺” assuming formation due to proton transfer with H₃⁺ and destruction by dissociative recombination with electrons and recombination on grain surfaces (using rates from Draine & Sutin 1987). The

abundance of H_3^+ is calculated considering formation as a consequence of cosmic ray ionization of molecular hydrogen and destruction by proton transfer with heavy molecules (essentially CO and N_2 here) as well as due to the processes mentioned above for molecular ions. We also consider metal ions M^+ formed by charge transfer and (including the equation for charge neutrality) solve a cubic equation for the electron abundance.

In similar fashion, we have computed the instantaneous $[\text{DCO}^+]/[\text{HCO}^+]$ (and $[\text{N}_2\text{D}^+]/[\text{N}_2\text{H}^+]$) ratios assuming that the respective deuterated species form by proton transfer from H_2D^+ . Thus, we express the abundance ratio $R_D = [\text{DCO}^+]/[\text{HCO}^+]$ as :

$$R_D = (1/3) k_1 x(\text{HD}) / (k_e x(e) + k_2 x(m) + k_3 x(\text{gr})). \quad (5)$$

In the above, k_1 is the rate for production of H_2D^+ due to reaction of HD with H_3^+ , k_e is the rate for dissociative recombination of H_2D^+ , k_2 is the rate coefficient for H_3^+ (and H_2D^+) destruction with neutral species, and k_3 is the rate for recombination of H_2D^+ on grain surfaces (Draine & Sutin 1987). $x(\text{HD})$ is the HD abundance relative to H_2 taken to be 3×10^{-5} (Linsky et al. 1995), $x(m)$, a function of the amount of depletion, is a weighted average over neutral molecules which can undergo proton transfer with H_3^+ , and $x(\text{gr})$ is the grain abundance by number. The latter has been computed (as has k_3) using a MRN (Mathis et al. 1977) distribution with lower cut-off radius a_{min} (100 Å in standard case) and upper cut-off 0.25 μm . This treatment ignores effects due to atomic deuterium (Dalgarno & Lepp 1984) and moreover assumes that all deuterium enrichment originates in H_2D^+ (rather than e.g. CH_2D^+). However, it improves on equation (1) of CWT98 in that it treats the depletion (via $x(m)$) in consistent fashion and in that it considers the effect of recombination on grains. From eqn. 5 it is clear that an increase of depletion boosts the deuterium fractionation. In fact, depletion causes a drop in the H_2D^+ and H_3^+ destruction rates, and a rise in the H_2D^+ formation rate, via $\text{H}_3^+ + \text{HD}$, due to the larger H_3^+ abundance. The net result is a larger $\text{H}_2\text{D}^+/\text{H}_3^+$ abundance ratio and a consequently more efficient deuterium fractionation.

In Fig. 4, we show the dependence on radius of various ionic and molecular abundances predicted by our standard models fitting the central CO column density of L1544 (left panels assume the density structure fit to the results of WMA, whereas the right hand panels were obtained assuming the density structure deduced by BAP). The top panels show predicted depletion factors for CO and N_2 . The bottom panels shows the electron fraction, and the predicted abundances for the various ionic species observed by us. We stress that this is *not* our “best fit” model (see Sect. 3.2.2) but it illustrates several features of our results.

We note first the rapid increase of the CO depletion factor with decreasing radius, i.e. the gaseous CO abundance is reduced to a value of order 10^{-3} (0.03) of the “canonical value” of 10^{-4} relative to H_2 in the constant density central region, using WMA (BAP) density values. This contrasts with N_2 which (although itself depleted) becomes the most abundant heavy molecule in the center. It is the rapid variation of these quantities as a function of density which renders necessary a consideration of abundance variations along the line of sight and hence radially. Also

shown in Fig. 4 are the variations of the DCO^+ and HCO^+ abundances. Their ratio (R_D) increases by roughly an order of magnitude from 0.04 (0.04) to 0.7 (0.35), using WMA (BAP) parameters, between the edge and center of our model.

The variation in ion densities shown in the bottom panel of Fig. 4 reflects the behavior of the depleted species in the two standard models. Thus, in a WMA core, HCO^+ abundance is strongly reduced in the center because of CO depletion, whereas DCO^+ shows a rather flat dependence due to the increase of the deuterium fractionation with increasing f_D . A similar behaviour is present for the N_2H^+ and N_2D^+ abundances, with the consequence that R_D and $[\text{N}_2\text{D}^+]/[\text{N}_2\text{H}^+]$ become greater than 1 in the innermost parts of the core. In a BAP core, the lower density causes less efficient CO and N_2 depletion, and much shallower profiles for HCO^+ and N_2H^+ fractional abundances. The ions plotted in the figure are “major ions” at all radii (except that H_3^+ becomes abundant in the central region under some circumstances) suggesting that for depleted high density cores, the sum of the observed molecular ion abundances may give a good estimate of the electron abundance. This is a great simplification relative to “normal cores” where “metal ions” have comparatively high abundances. Our calculations suggest that in high density depleted cores, the depletion of “metals” (assumed here to behave like CO) is likely to be so large that this complication becomes negligible. We have used an initial metal abundance about one order of magnitude lower than that measured in diffuse clouds, as is usual (“low metals”) in chemical models of dense clouds (e.g. Prasad & Huntress 1982; Herbst & Leung 1989; Graedel et al. 1982; Lee et al. 1996).

The most convincing aspect of our model is that it qualitatively explains the enhancement of N_2D^+ in the center of L1544, close to the depletion peak. Thus it explains the higher degree of fractionation of deuterium in N_2D^+ as compared with HCO^+ . It also explains roughly the differing depletions observed for N_2H^+ , CO, and HCO^+ . In fact, as discussed in the next section, the qualitative features of the model are in excellent agreement with observation. The pattern that ions and deuterated species peak close to dust emission maxima appears to be a general feature (Tafalla et al., in prep.) of nearby cores and suggests that the model presented here has wider applications than to L1544.

3.2.2. *The best fit model*

Several model calculations have been performed to find the “best fit model”, i.e. the model which best reproduces observed column densities at the peak of L1544. We started with a “standard” cloud model, where $\zeta = 1.3 \times 10^{-17} \text{ s}^{-1}$, the CO binding energy $E_D(\text{CO}) = 1210 \text{ K}$ (Hasegawa et al. 1992), the N_2 binding energy $E_D(\text{N}_2) = 787 \text{ K}$, the minimum radius of dust grains $a_{\text{min}} = 10^{-6} \text{ cm}$, the sticking coefficient $S = 1.0$ (see Table 2). Two density distributions

(from WMA and BAP) were considered and the above parameters were varied until the quantity:

$$\chi^2 = \sum_{i=1}^4 \left[\frac{1}{\sigma_{N_{\text{obs}}(i)}} (N_{\text{obs}}(i) - N_{\text{mod}}(i)) \right]^2 \quad (6)$$

was minimised. In eqn.(6), $N_{\text{obs}}(i)$ and $N_{\text{mod}}(i)$ are the observed and model calculated column density of HCO^+ , DCO^+ , N_2H^+ , and N_2D^+ at the L1544 “molecular peak”. $\sigma_{N_{\text{obs}}(i)}$ is the uncertainty associated with $N_{\text{obs}}(i)$, which has been assumed here to be a 30% error. Thus we assume the errors in our column density determination to be dominated by systematic effects such as those caused by our summary treatment of the radiation transfer.

The column density dependence as a function of impact parameter b predicted by the two “best fit” models (for the two density distributions) can then be compared with those observed. We have made azimuthal averages of our observed column densities using averages within bins defined by $i < b < i + 20$ arcsec, with $i = 0, 20, 40, \dots$ (arcsec), with the exception of the value at $b = 0$. This is shown in Fig. 5, where large symbols represent the average column density inside the corresponding bin (symbols mark the upper edge of each bin). One sees that there is considerable scatter as indeed one can expect given the elongated nature of the maps. This is in particular the case for N_2H^+ where the “mean” calculated in this fashion may clearly be misleading. One sees nevertheless that the distributions become clearly more peaked going from CO (flat) to N_2D^+ .

In Fig. 6, the observed column density profiles are compared with those predicted by four models compatible with the peak column densities. The parameters used in these models are reported in Tab. 2 together with the χ -squared estimates using equation (6). To understand our results, it is useful to recall that we need to assume high degrees of CO depletion in order to explain the CO and HCO^+ column densities. A certain amount of nitrogen depletion is also needed to explain $\text{N}(\text{N}_2\text{H}^+)$. Such low gas phase molecular abundances cause extremely high degrees of D fractionation however with the model expectation for e.g. $[\text{DCO}^+]/[\text{HCO}^+]$ higher than unity in the dense depleted central regions. This then gives difficulty explaining the abundances of N_2D^+ and N_2H^+ . The range of parameters in Tab. 2 demonstrates that the peak column densities on their own only give partial constraints on the chemical models.

Fig. 6 however shows that the extent of the emission in the various ions is also an important constraint. In models 1 and 2 (Tab. 2) for example, the model half-width for N_2H^+ is much too small. While this could be partially due to our azimuthal averaging (see Fig. 5), it is also the case that the cosmic ray ionization rate has been chosen to have values in models 1 and 2 more than an order of magnitude lower than in the standard model and the result is that $\text{N}(\text{N}_2\text{H}^+)$ is much too small at large radii.

A way of improving the agreement between observations and model predictions is to more efficiently deplete CO outside the core center (to increase the N_2H^+ column density at $b > 0$). This can be done by increasing the CO binding energy and thus reducing the efficiency of cosmic ray induced desorption. However, this also causes an increase in deuterium fractionation which is not observed. As discussed in Sect. 2.4.1, $[\text{DCO}^+]/[\text{HCO}^+]$ is observed to have rather low values

at high impact parameter. This suggests that reactions other than with CO and N₂ act to reduce the H₂D⁺ abundance. We therefore postulate the existence of a volatile neutral species which will remain in the gas phase when CO is depleted and which has a proton affinity permitting transfer of a proton from H₃⁺.

This species needs to be abundant (at least as abundant as CO) to effectively keep the deuterium fractionation low in those regions where CO is significantly depleted. One possibility may be atomic oxygen, which is predicted to be quite abundant in dense clouds (e.g. Lee et al. 1996; Bergin et al. 2000; Viti et al. 2001). Its binding energy onto a dust grain covered with water ice is thought to be a factor of about 1.5 smaller than that of CO ($E_D(\text{O}) \sim 800$ K; Tielens & Allamandola 1987). We have therefore run several models which include atomic oxygen in the chemistry, with different values of $E_D(\text{O})$, and determine the χ^2 and column density profiles in the same fashion as before. These results are shown in Fig. 7 and correspond to models 3 and 4 of Table 2. One sees that model 3 in particular gives a reasonable fit although the DCO⁺ column density profile is still somewhat deviant. Both models 3 and 4 require an oxygen binding energy of ~ 600 K.

Using the “best fit” models in Tab. 2, namely Models 1 and 3, we determined the variation of the electron fraction with cloud radius r . Fig. 8 shows the fractional abundance of electrons, HCO⁺, DCO⁺, N₂H⁺, and N₂D⁺, as well as the depletion factor f_D , as a function of r . Model 3 (the best fit model) predicts a $[\text{N}_2\text{D}^+]/[\text{N}_2\text{H}^+]$ abundance ratio equal to ~ 0.4 at radius $r \sim 2500$ AU. Both models show $x(e)$ between $\sim 10^{-9}$ at $r \sim 2500$ AU ($n(\text{H}_2) \sim 10^6 \text{ cm}^{-3}$) and $\sim 10^{-8}$ at $r \sim 10^4$ AU ($n(\text{H}_2) = \text{a few} \times 10^4 \text{ cm}^{-3}$). In these models, the dependence of $x(e)$ upon gas density $n(\text{H}_2)$ is approximately given by :

$$x(e) = 6.3 \times 10^{-6} \times n(\text{H}_2)^{-0.64},$$

in Model 1, and

$$x(e) = 5.2 \times 10^{-6} \times n(\text{H}_2)^{-0.56},$$

in Model 3. These estimates are roughly an order of magnitude lower than the standard relation between $x(e)$ and $n(\text{H}_2)$ ($x(e) = 1.3 \times 10^{-5} \times n(\text{H}_2)^{-0.5}$; McKee 1989). In other words, our results are compatible with electron fractions only a factor of order 3 higher than the lower limits based on the inferred HCO⁺ abundance in the nucleus of L1544. Such low electron fractions are linked to the depletion of metals which, being positively charged, directly affect the electron budget of cloud cores. We use an initial abundance of metals 10 times lower than in the standard relation quoted above and this causes the difference in the coefficient (see Sect. 3.2.1). The difference in the exponent is to be attributed to the further metal depletion inside the core. If larger initial metal abundances are used, $x(e)$ increases at the outer edges of the core, but it does not significantly change at the core center, where metal abundances are negligible because of depletion. In this case, a steeper slope in the $x(e) - n(\text{H}_2)$ relation is obtained. We caution that these estimates have large uncertainty as the differences in the models of Tab. 2 shows. Our approach to inferring

molecular ion densities as a function of radius is questionable and the real geometry is non spherically symmetric. There are additionally many uncertainties in the chemistry. Nevertheless, we conclude tentatively that the “standard relationship” may give a considerable over–estimate of the electron fraction in L1544. This has consequences for the ambipolar diffusion timescale.

In the central portion of L1544, ionization degrees of the order of 10^{-9} imply an ambipolar diffusion time scale of roughly $2.5 \times 10^{13} x(e) = 2.5 \times 10^4$ yrs (see Spitzer 1978 and Shu et al. 1987), comparable to the free–fall time scale at densities of $\sim 10^6 \text{ cm}^{-3}$. This is consistent with the view that within the central region, (see Ciolek and Basu 2001, Ciolek and Basu 2000), conditions are “super–critical” and the core is rapidly developing towards a situation where it will collapse. However, the “caveats” noted above mean that one needs to test this conclusion with observations capable of better delineating the structure of the high density nucleus of L1544.

3.2.3. Chemical problems with the best fit model

There are some problems related with the existence of atomic oxygen in the gas phase which need to be clarified. In our models, the large abundance of gaseous O is due to the low value of $E_D(\text{O})$ and to the cosmic ray desorption mechanism which allows a prompt return of this species to the gas phase, once adsorbed onto grain surfaces. We are neglecting here the fact that the reactions of atomic oxygen with H_3^+ necessary to reduce deuterium fractionation will also produce water and OH in the gas phase which can then deplete out onto grains, although only a small fraction of O (< 0.01) will be lost due to this process (e.g. Lee et al. 1996). An important consequence of the $\text{H}_3^+ + \text{O}$ reaction is that H_3O^+ becomes the most abundant molecular ion in the depleted core ($x(\text{H}_3\text{O}^+) \sim 10^{-9}$ at $n(\text{H}_2) \sim 10^6 \text{ cm}^{-3}$ as also found by Aikawa et al. 2001). However, the destruction rate of atomic oxygen through reactions with H_3^+ ($r_{\text{H}_3^+}$) is significantly slower than the O accretion rate onto dust grains (r_{dust})². This means that if the accreted O will not be completely processed onto grain surfaces, through, say, hydrogenation leading to water, between successive cosmic ray bombardments, we expect a fraction of free oxygen to be maintained on the gas phase. Proving the validity of these assumptions is outside the scope of this paper but we consider briefly the likely chemistry of atomic O on grain surfaces.

Following Hasegawa & Herbst 1993 (see Léger et al. 1985), if the major source of nonthermal grain heating is due to Fe nuclei with energies 20–70 MeV nucleon⁻¹, the time interval between successive cosmic ray impacts is about 10^6 years. If the fractional abundance of atomic oxygen is $\sim 10^{-4}$ and $n(\text{H}) \sim 1 \text{ cm}^{-3}$, as gas phase models of dense clouds predict at steady state for

²At a density of $\sim 10^6 - 10^5 \text{ cm}^{-3}$, our best fit model predicts $x(\text{H}_3^+) \sim 1 - 2 \times 10^{-10}$, so that $r_{\text{H}_3^+} = k_{\text{H}_3^+} \times x(\text{H}_3^+) \times n(\text{H}_2) \sim 1 - 2 \times 10^{-14} \text{ cm}^{-3}\text{s}^{-1}$, where the rate coefficient $k_{\text{H}_3^+} \sim 10^{-9} \text{ cm}^3 \text{ s}^{-1}$. For the O accretion rate, assuming a unity sticking coefficient and dust grains of 10^{-5} cm in size, $r_{\text{dust}} \sim 10^{-17} n(\text{H}_2) \text{ cm}^{-3}$, implying $r_{\text{dust}}/r_{\text{H}_3^+} \sim 50 - 100$ at $n(\text{H}_2) = 10^5 - 10^6 \text{ cm}^{-3}$, respectively.

$\zeta = 10^{-17} \text{ s}^{-1}$ (e.g. Lee et al. 1996), $T = 10 \text{ K}$, and $n(\text{H}_2) \sim 10^5 \text{ cm}^{-3}$, the O and H accretion rates are $\sim 4 \times 10^{-5} \text{ s}^{-1}$ and $1 \times 10^{-5} \text{ s}^{-1}$, respectively, i.e. between two cosmic ray bombardments about 10^9 O and 3×10^8 H atoms can accrete on the surface of a grain. Assuming that hydrogen can quickly move on the grain surface (from the laboratory work of Katz et al. 1999, the H diffusion rate on silicate grains is about $2 \times 10^{-4} \text{ s}^{-1}$, much larger than the c.r. heating rate), a fraction between 15% and 30% of surface O will be hydrogenated and transformed in OH and H_2O . The rest of the O atoms may form O_2 , but observations have shown that this is probably not the main repository of oxygen either in the solid (Vandenbussche et al. 1999) or in the gas phase (Goldsmith et al. 2000). It is thus possible that a large fraction of atomic oxygen remains unreacted on the grain before the next cosmic ray will release it back in the gas phase.

It is relevant in this contest that the detailed gas–grain chemical–dynamical model of L1544, presented by Aikawa et al. 2001 (which includes depletion onto dust grains but no surface processing of accreted species) predicts large O fractions across the core (from $\sim 10^{-4}$ at $n(\text{H}_2) \sim 10^5 \text{ cm}^{-3}$ to a few $\times 10^{-5}$ at 10^6 cm^{-3} , similar to our results). This is in their “fast collapse” model, which fits the observed CCS and CO distributions. Our model is crude compared with that of Aikawa et al. 2001, but nevertheless both models reproduce the observed features quite well, proving the validity of our chemical assumptions in Sect. 3.2.1. There are some differences between the two models concerning the prediction of N_2H^+ and N_2D^+ abundances. In Aikawa et al. 2001, the calculated column densities of the two species are smaller than those observed by about an order of magnitude, perhaps due to uncertainties in the N_2 formation mechanism. We “avoid” this problem by simply starting the chemistry with all the available nitrogen already in the form of gas phase N_2 (Sect. 3.2.1), thus reproducing the observed N_2H^+ and N_2D^+ column density variations (see Model 3 in Fig. 6).

4. Conclusions

An important result of this study is that N_2H^+ shows more deuterium fractionation towards the dust emission peak of L1544 than HCO^+ (models without depletion gradients expect $[\text{DCO}^+]/[\text{HCO}^+] = [\text{N}_2\text{D}^+]/[\text{N}_2\text{H}^+]$ Rogers and Charnley 2001). We suspect that the high degree of deuteration observed in ammonia (see Tiné et al. 2000, Roueff et al. 2000) in some cores can be best explained by a model similar to that which we have adopted. Ammonia like N_2H^+ is easily produced from N_2 (see Rogers and Charnley 2001) and is therefore likely to be relatively abundant in the depleted region. The compact nature of “ammonia cores” is naturally explained if this is the case (Tafalla et al., in prep.).

We have attempted to obtain density estimates for the regions within the L1544 core giving rise to the observed DCO^+ and $\text{N}_2\text{H}^+(\text{N}_2\text{D}^+)$ emission. We obtain in this way values between 10^5 and 10^6 cm^{-3} consistent with the general idea that we are observing selectively the high density layers. The results from DCO^+ suggest densities as high as 10^6 cm^{-3} consistent with the values inferred from dust emission and absorption. However, lower values are obtained based upon our

N_2H^+ and N_2D^+ data. This is surprising and we are presently unsure of the explanation. The observed spatial distribution suggests that N_2H^+ and N_2D^+ reside in higher density layers than DCO^+ . The reasons for this discrepancy could have to do with the isothermal assumption which we have made based upon our C^{18}O and NH_3 results. Attempts to simulate the dust emission from L1544 (Zucconi et al. 2001, Evans et al. 2001) have shown that there is probably a substantial fall off in dust temperature from the center to the edge with values of order 7 K in the nucleus. At densities above 10^5 cm^{-3} (Krügel and Walmsley 1984) gas and dust temperatures are probably coupled and hence there may be a gradient in the gas temperature too (see also Goldsmith 2001). This should be taken into account in future studies.

We have developed a crude model of the ion–chemistry in the core of L1544. This simulates the observed depletion and can reproduce the observed dependence of the column densities of species such as N_2H^+ , N_2D^+ , HCO^+ , and DCO^+ as a function of offset. The main advantage of this is that it allows us in objective fashion to consider the relative contributions to observed column densities from the high density depleted nucleus and the lower density foreground (background) gas. There are large uncertainties in both the input to the chemistry and the process of inferring radial dependences of molecular abundances from the observations. One interesting result is that we get the best fit to the observed deuterium fractionation in models in which atomic oxygen is allowed to remain with an abundance of order 10^{-4} in the gas phase. There are some problems associated with this but one needs more detailed models of both the surface and gas phase chemistry to test this. It does have an observational consequence which is that H_3O^+ becomes a major ion towards the dust peak, in agreement with numerical chemical models of Aikawa et al. 2001.

Applying this model, we find that the ionization degree in L1544 is likely to be an order of magnitude smaller than estimated using “canonical formulae” existing in the literature, mainly because of the reduced metal abundances. The result is a tentative finding because we have difficulty in fitting the observed abundances as a function of offset in L1544 and in particular the observed degree of D fractionation. However, our estimates for ionization degree do not vary greatly when one compares the different models which give an adequate fit to the observed column density distributions. We conclude that in the case of L1544, the ionization degree is lower and hence the ambipolar diffusion timescale is shorter. Our estimated timescale is of the same order as the free-fall time consistent with the idea that the nucleus of the L1544 core is undergoing dynamical collapse.

A final point to emphasize is that in models without atomic oxygen, or where O also experiences strong depletion, the main ion in the highly depleted region is H_3^+ , so that the mean mass of positive ions decreases from ~ 30 (in the “canonical” undepleted case, where the representative ion is HCO^+) to ~ 3 . This has the consequence of further reducing the ambipolar time scale, due to a drop in the drag coefficient, by a factor of 7–8 (D. Galli, priv. comm.).

Other cores may yield different results and the effects of the possible temperature gradient mentioned above need to be taken into account. Finally, it will be important in future studies to

take into account a more realistic geometry (non spherically symmetric) than we have done.

The authors are grateful to the referee, Neal Evans, for useful comments and suggestions. PC and CMW wish to acknowledge travel support from ASI Grants 66-96, 98-116, as well as from the MURST project “Dust and Molecules in Astrophysical Environments”. We are grateful to Daniele Galli for providing the subroutine for the calculation of the electron fraction.

A. Column density determination

In addition to the LVG calculations, we also used the following expressions to determine the total column density. For optically thick transitions:

$$N_{\text{TOT}} = \frac{8\pi^{3/2}\Delta v}{2\sqrt{\ln 2}\lambda^3 A} \frac{g_l}{g_u} \frac{\tau}{1 - \exp(-h\nu/kT_{\text{ex}})} \frac{Q_{\text{ROT}}}{g_l \exp(-E_l/kT_{\text{ex}})}, \quad (\text{A1})$$

where Δv is the line width, λ and ν are the wavelength and frequency of the observed transition, respectively, A is the Einstein coefficient, g_l and g_u are the statistical weight of the lower and upper levels, τ is the optical depth, h is Planck constant, T_{ex} is the excitation temperature (assumed the same for all rotational levels), Q_{ROT} is the partition function, E_l is the energy of the lower level, and k is Boltzmann constant. For linear molecules (as those observed in this paper):

$$Q_{\text{ROT}} = \sum_{J=0}^{\infty} (2J+1) \exp[-E_J/(kT)] \quad (\text{A2})$$

$$E_J = J(J+1)hB, \quad (\text{A3})$$

where J is the rotational quantum number, and B is the rotational constant. For rotational transitions with hyperfine structure (e.g. $\text{N}_2\text{H}^+(1-0)$ and $\text{N}_2\text{D}^+(2-1)$), τ refers to the total optical depth (given by the sum of the peak optical depths of all the hyperfine components), and Δv to the intrinsic line width. The error on N_{TOT} is given by propagating the errors on Δv , τ , and T_{ex} in eqn. A1.

If a line is optically thin and all the rotational levels are characterized by the same excitation temperature T_{ex} , the expression of the total column density becomes:

$$N_{\text{TOT}} = \frac{8\pi W}{\lambda^3 A} \frac{g_l}{g_u} \frac{1}{J_\nu(T_{\text{ex}}) - J_\nu(T_{\text{bg}})} \frac{1}{1 - \exp[-h\nu/(kT_{\text{ex}})]} \frac{Q_{\text{ROT}}}{g_l \exp[-E_l/(kT_{\text{ex}})]}, \quad (\text{A4})$$

where W is the integrated intensity of the line ($W = \sqrt{\pi}/(2\sqrt{\ln 2}) \times \Delta v T_{\text{mb}}$, for a gaussian line, with $T_{\text{mb}} \equiv$ main beam brightness temperature), $J_\nu(T_{\text{ex}})$ and $J_\nu(T_{\text{bg}})$ are the equivalent Rayleigh–Jeans excitation and background temperatures. The integrated intensity of each line has been measured by integrating over a velocity range determined in the following way: (i) sum all the spectra in the map; (ii) find the *rms*, or the 1σ level of the noise in the off–line channels of the sum spectrum; (iii) include in the velocity range for integration (at zero level) all the channels in the line which are above the 1σ level determined in point (ii). For the calculation of the total column density only those positions with $W/\sigma_W \geq 3$ have been considered (σ_W is the error on W , determined by the expression $\sigma_W = \Delta v_{\text{res}} \times \text{rms} \times \sqrt{N_{\text{ch}}}$, where Δv_{res} is the spectral resolution in km s^{-1} , and N_{ch} is the number of channels in the integrated area). The error on N_{TOT} is simply given by $\sigma_{N_{\text{TOT}}} = \sigma_W \times N_{\text{TOT}}/W$,

The parameters used to determine N_{TOT} for each species are listed in Table 1.

A.1. DCO⁺ and HCO⁺

As we saw in Sect. 2.2, an LVG statistical equilibrium code has been used to estimate number density and DCO⁺ column density from observed DCO⁺(3–2) and (2–1) lines. To quantify the uncertainties in column density estimates from statistical equilibrium (SE) calculations, due to the unknown DCO⁺ fractional abundance and H₂ number density, we first determined DCO⁺ column densities from the SE code and a least square method applied to model calculated data points. To do this, the SE program was run for different values of H₂ number density (between 10³ and 10⁶ cm⁻³) and DCO⁺ fractional abundances (between 10⁻¹² and 10⁻⁹). Each run furnishes a value of T_{ex} , τ , T_{mb} of the first four rotational transitions of DCO⁺, together with the DCO⁺ column density divided by line width. Secondly, a least-square method was applied to these model data points to find general expressions for estimating $N(\text{DCO}^+)$ once the brightness temperature $T_{\text{mb}(2-1)}$ of the J = 2-1 line and the $W(\text{DCO}^+(3-2))/W(\text{DCO}^+(2-1))$ ($\equiv R_W$) integrated intensity ratio are known from observations. However, this gives $N(\text{DCO}^+)$ values with associated errors greater than 30% ($N/\sigma_N < 3$), so we decided to first determine the excitation temperature ($T_{\text{ex}(2-1)}$) and the optical depth ($\tau_{(2-1)}$) of the J = 2–1 line using the least-square method, which gives:

$$T_{\text{ex}(2-1)} = a_1 + a_2 \log R_W + a_3 T_{\text{mb}}(2-1) \quad (\text{A5})$$

$$\log \tau_{(2-1)} = b_1 + b_2 (\log R_W)^2 + b_3 \log(T_{\text{mb}}(2-1)), \quad (\text{A6})$$

with $a_1 = 11.3 \pm 0.1$, $a_2 = 10.3 \pm 0.2$, $a_3 = -0.05 \pm 0.01$, $b_1 = -0.2 \pm 0.1$, $b_2 = 2.0 \pm 0.5$, $b_3 = 1.0 \pm 0.1$. Secondly, we assumed $T_{\text{ex}} = T_{\text{ex}(2-1)}$ for all rotational levels, and finally calculate N using expressions (A4) or (A1) in the appendix, depending on the value of the optical depth ($\tau_{(2-1)} < \text{or} > 0.5$, respectively). Only positions inside the half maximum contour of the DCO⁺(2–1) integrated intensity map have been included in this calculation, to exclude low sensitivity spectra from the analysis. The particular form of these expressions was chosen because of the relatively low χ^2 . If from (A6) $\tau/\sigma_\tau < 3$, $\tau_{(2-1)}$ was estimated from the radiative transfer equation

$$\tau = -\log \left[1 - \frac{T_{\text{mb}}}{J_\nu(T_{\text{ex}}) - J_\nu(T_{\text{bg}})} \right], \quad (\text{A7})$$

where $J_\nu(T_{\text{ex}})$ and $J_\nu(T_{\text{bg}})$ are the equivalent Rayleigh-Jeans excitation and background temperatures, and T_{ex} is given by eqn. (A5). Finally, if the resultant $N/\sigma_N < 3$, T_{ex} was fixed to 7 K, its mean value³, and τ estimated from (A7). $T_{\text{ex}} = 7$ K was also assumed for all the positions outside the half maximum contour of the DCO⁺(2–1) integrated intensity map, where eqns. (A5) and (A6) cannot be applied because of the poor R_W estimate. In the particular case of the (20, -20) offset position, the optically thin D¹³CO⁺(2–1) line was used to estimate the DCO⁺ column density, assuming the same excitation temperature found for the DCO⁺(2–1) line. *We note that*

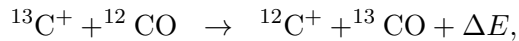
³ T_{ex} drops from ~ 9 K towards the map peak, at offset (20, -20), and two adjacent positions to $\lesssim 7$ K at larger distances from the peak.

the different approaches used in estimating column densities do not change the results by more than a factor of 2. However, it is important to estimate the optical depth of the line before determining the column density. For example, in the case of offset (20, -20) where the $\text{DCO}^+(2-1)$ line has one of the largest values of optical depth (~ 2), (i) the SE calculation together with equation (A1) give $N(\text{DCO}^+) = (4\pm 1)\times 10^{12} \text{ cm}^{-2}$, (ii) the use of $T_{\text{ex}} = 7 \text{ K}$ and eqn.(A7), gives $\tau = 1.7\pm 0.2$ and $N(\text{DCO}^+) = (2.0\pm 0.2)\times 10^{12} \text{ cm}^{-2}$, and (iii) the use of $\text{D}^{13}\text{CO}^+(2-1)$ leads to $N(\text{DCO}^+) = (4.0\pm 0.3)\times 10^{12} \text{ cm}^{-2}$. If the optical depth of the $\text{DCO}^+(2-1)$ line is not taken into account, one obtains $N(\text{DCO}^+) = (9.6\pm 0.2)-(10.2\pm 0.2)\times 10^{11} \text{ cm}^{-2}$, if $T_{\text{ex}} = 7 - 9 \text{ K}$, respectively.

For the determination of the HCO^+ column density, the excitation temperature was assumed equal to that found for DCO^+ . We used the optically thin $\text{HC}^{18}\text{O}^+(1-0)$ line, if available, and the $\text{H}^{13}\text{CO}^+(1-0)$ line in all other positions. The passage from $N(\text{HC}^{18}\text{O}^+)$ and $N(\text{H}^{13}\text{CO}^+)$ to $N(\text{HCO}^+)$ was made by multiplying the former quantities by 560 and 77, respectively, based on the $^{16}\text{O}/^{18}\text{O}$ and $^{12}\text{C}/^{13}\text{C}$ abundance ratios in the local ISM (Wilson & Rood 1994).

The optical depth of $\text{H}^{13}\text{CO}^+(1-0)$ was calculated from eqn. (A7). As in the case of DCO^+ , eqn.(A4) or (A1) was used, depending on the value of τ . It is interesting to note that the resultant τ in many positions is less than 0.5, i.e. $\text{H}^{13}\text{CO}^+(1-0)$ is mostly optically thin and thinner than the $\text{DCO}^+(2-1)$ line in the central part of the core. However, the profile of $\text{H}^{13}\text{CO}^+(1-0)$ suggests the existence of absorption by a low density foreground layer (see Tafalla et al. 1998, Williams et al. 1999) which may cause a decrease in the brightness temperature and, consequently, in the line optical depth (see eqn. A7). The three hyperfine components of the $\text{HC}^{17}\text{O}^+(1-0)$ transition detected at offset (20, -20), and shown in Dore et al. 2001 together with their recent measurement in the laboratory, allowed us to check the thickness of the $\text{HC}^{18}\text{O}^+(1-0)$ line. Assuming $T_{\text{ex}} = 9 \text{ K}$, the excitation temperature found from DCO^+ data at the same position, we find $N(\text{HC}^{18}\text{O}^+)/N(\text{HC}^{17}\text{O}^+) = 4.2\pm 0.4$, quite close to the $^{18}\text{O}/^{17}\text{O}$ ratio ($= 3.65$; Penzias 1981) expected in optically thin conditions.

The determination of the HCO^+ column density starting from H^{13}CO^+ is affected by an additional complication, i.e. the presence of ^{13}C fractionation in cold and dense gas (e.g. Smith & Adams 1984) due to the exothermic reaction:



with $\Delta E/k = 35 \text{ K}$ (Watson 1977). In optically thin conditions, the $N(\text{H}^{13}\text{CO}^+)/N(\text{HC}^{18}\text{O}^+)$ column density ratio should be equal to the product of $^{13}\text{C}/^{12}\text{C}$ and $^{16}\text{O}/^{18}\text{O}$ abundance ratios (~ 7). In L1544, $N(\text{H}^{13}\text{CO}^+)/N(\text{HC}^{18}\text{O}^+)$ ranges from 3 (at offset [80, -80]) to 7 (at offset [40, -80]) with an average value of 4 ± 1 . It is thus always lower than the local interstellar medium value, suggesting that ^{13}C fractionation is not significantly affecting our conclusions. However, given that $\text{H}^{13}\text{CO}^+(1-0)$ is probably affected by foreground absorption, it is extremely hard to estimate the effects of ^{13}C fractionation. From the current data we determined the $W[\text{H}^{13}\text{CO}^+(1-0)]/W[\text{HC}^{18}\text{O}^+(1-0)]$ integrated intensity ratio and found an average value of 4 ± 1 , smaller than the value expected in optically thin conditions and no ^{13}C fractionation. This

result suggests that optical depth effects on the $\text{H}^{13}\text{CO}^+(1-0)$ line are in any case predominant.

A.2. CO

For the CO column density, we used $\text{C}^{17}\text{O}(1-0)$, when available, and $\text{C}^{18}\text{O}(1-0)$ in the other positions assuming $T_{\text{ex}} = 10$ K (Sect. 2.1), $[\text{C}^{17}\text{O}]/[\text{C}^{16}\text{O}] = 2044$, and $[\text{C}^{18}\text{O}]/[\text{C}^{16}\text{O}] = 560$ (Wilson & Rood 1994, Penzias 1981). $\text{C}^{17}\text{O}(1-0)$ has (well resolved) hyperfine components with relative intensity ratios consistent with optically thin emission, whereas $\text{C}^{18}\text{O}(1-0)$ has a moderate optical depth (τ between 0.5 and 1), based on the comparison between the $W(\text{C}^{18}\text{O}(1-0))/W(\text{C}^{17}\text{O}(1-0))$ integrated intensity ratio and the $[\text{C}^{18}\text{O}]/[\text{C}^{17}\text{O}]$ abundance ratio in the local ISM. Following Myers et al. 1983, we derive:

$$\frac{T_{\text{mb}}[\text{C}^{18}\text{O}(1-0)]}{T_{\text{mb}}[\text{C}^{17}\text{O}(1-0)]} = 3.65 \times \left(\frac{1 - \exp(-\tau_{18})}{\tau_{18}} \right), \quad (\text{A8})$$

where $T_{\text{mb}}(i)$ is the main beam brightness temperature of line i and τ_{18} is the $\text{C}^{18}\text{O}(1-0)$ optical depth. Once τ_{18} is known from the above equation, the excitation temperature of the C^{18}O line can be determined from the radiative transfer equation:

$$T_{\text{ex}} = \frac{h\nu/k}{\ln\left(\frac{h\nu}{kJ\nu(T_{\text{ex}})} + 1\right)}, \quad (\text{A9})$$

where ν is the frequency of the $\text{C}^{18}\text{O}(1-0)$ line. The variation in T_{ex} from point to point in the map is not significant, considering the errors, and we assumed a constant value of T_{ex} ($= 10$ K) given by the weighted mean of the excitation temperature in the observed positions. As in the case of $N(\text{DCO}^+)$ and $N(\text{H}^{13}\text{CO}^+)$, when $\tau > 0.5$, the C^{18}O column density has been calculated using eqn. (A1).

A.3. N_2H^+ and N_2D^+

The observed $\text{N}_2\text{H}^+(1-0)$ and $\text{N}_2\text{D}^+(2-1)$ lines present hyperfine structure due to the interaction between the molecular electric field gradient and the electric quadrupole moments of the two nitrogen nuclei. The $J = 1 \rightarrow 0$ line of N_2H^+ is splitted in seven components (see Caselli et al. 1995), whereas $\text{N}_2\text{D}^+(2-1)$ has 38 hyperfines which partially overlap because of line broadening.

We first determined the intrinsic linewidth, total optical depth, and excitation temperature from the hfs fitting procedure applied to high sensitivity spectra (selected by requiring $W/\sigma_W > 20$, W being the intensity integrated under the seven hyperfine components). In fact, the optical depth determination becomes more and more uncertain with increasing spectral rms, which can alter the relative intensities of the components and thus crucially affect τ estimates. Therefore it is important to have clear detections of the seven components before attempting an hfs fit.

However, even in the presence of high sensitivity spectra one can encounter problems if the transition is very thick ($\tau \geq 30$) because the CLASS fit procedure is limited to τ values smaller than 30. In these cases, it is convenient to estimate the $\text{N}_2\text{H}^+(1-0)$ optical depth from the thinnest component (the lowest frequency $J_{F_1,F} = 1_{1,0} \rightarrow 0_{1,1}$ line, see Caselli et al. 1995) assuming a certain value of T_{ex} (e.g. the mean value, $\langle T_{\text{ex}} \rangle$, which in L1544 is 5 K), and using eqn. A7. The hfs fit gives $\tau = 30$ - with a suspiciously low associated error (~ 0.1) - in four positions of the L1544 $\text{N}_2\text{H}^+(1-0)$ map (offsets [40, -40], [20, -40], [40, -60], and [20, -60]). For these spectra, the use of eqn. A7 with $T_{\text{ex}} = 5$ K confirms the presence of high optical depth (≤ 30). In these cases, we used the integrated intensity of the “weak” and moderately thick ($\tau_{1,0-1,1} \leq 1$) $F_1, F = 1,0 \rightarrow 1,1$ component to determine the total N_2H^+ column density from eqn.(A4). Although this may underestimate the total column density by a factor of $\sim \tau/(1 - \exp(-\tau)) \leq 1.6$, the uncertainty associated on the above estimate of the total optical depth is also large (about 20%), and does not take into account of the possible presence of excitation anomalies, as found by Caselli et al. 1995. For consistency, the use of the $F_1, F = 1,0 \rightarrow 1,1$ component to estimate the total N_2H^+ column density has been extended to all other positions where this hyperfine is well detected.

For those $\text{N}_2\text{H}^+(1-0)$ spectra which cannot be hfs fitted because of low sensitivity, and where the “weak” component is not visible, we assumed optically thin conditions, $T_{\text{ex}} = 5$ K, and determined $N(\text{N}_2\text{H}^+)$ using eqn. A4.

As we already pointed out at the beginning of this section, the $J = 2 \rightarrow 1$ transition of N_2D^+ is splitted in 38 hyperfine components and only in one position (the integrated intensity map peak, where the $\text{N}_2\text{D}^+(2-1)$ observations have been repeated several times to check the system) it has been possible to determine the total optical depth and excitation temperature from the hfs fit ($\tau_{\text{tot}} = 4.9 \pm 0.6$, $T_{\text{ex}} = 4.9 \pm 0.8$ K). In all the other positions we (i) assumed optically thin conditions, (ii) estimated the integrated intensity below the hyperfines (W) with its uncertainty (σ_W), (iii) excluded all spectra with $W/\sigma_W < 3$, (iv) fixed T_{ex} at 5 K, and (v) use eqn. (A4) to estimate the total column density.

REFERENCES

- Aikawa Y., Ohashi N., Inutsuka S., Herbst E., Takakuwa S. 2001, ApJ, 552, 639
- Anderson I. M., Caselli P., Haikala L. K., Harju J. 1999, A&A, 347, 983
- Bacmann A., André P., Puget J. -L., Abergel A., Bontemps S., Ward-Thompson D. 2000, A&A, 361, 555(BAP)
- Benson P. J., Myers P. C. 1989, ApJS, 71, 89
- Bergin E. A., Ciardi D. R., Lada C. J., Alves J., Lada E. A. 2001, ApJ, in press

- Bergin E. A., Langer W. D. 1997, ApJ, 486, 316
- Bergin E. A., Melnick G. J., Stauffer J. R., et al. 2000, ApJ, 539, L129
- Bergin E. A., Plume R., Williams J. P., Myers P. C. 1999, ApJ, 512, 724
- Botschwina P. 1989 in *Ion and Cluster Spectroscopy*, edited J.P.Maier, publ. Elsevier
- Butner, H. M., Lada, E. A., Loren, R. B. 1995, ApJ, 448, 207
- Caselli P., Hasegawa T. I., Herbst E. 1998, ApJ, 495, 309
- Caselli P., Myers P. C., Thaddeus P. 1995, ApJ, 455, L77
- Caselli P., Walmsley C. M., Tafalla M., Dore L., Myers P. C. 1999, ApJ, 523, L165 (CWT99)
- Caselli P., Walmsley C.M., Terzieva R., Herbst E. 1998 ApJ, 499, 234 (CWT98)
- Ciolek, G.E., Basu S 2000 ApJ 529, 925
- Ciolek G.E., Basu S. 2001, ApJ, 547, 272
- Dalgarno A., Lepp S. 1984, ApJ, 287, L47
- Dore L., Cazzoli G., Caselli P. 2001, A&A, 368, 712
- Draine B. T., Sutin B. 1987, ApJ, 320, 803
- Evans N.J. II, Rawlings J.M.C., Shirley Y., Mundy L.G. 2001, ApJ, in press
- Flower D. R. 1999, MNRAS, 305, 651
- Frerking M. A., Langer W. D., Wilson R. D. 1982, ApJ, 262, 590
- Goldsmith P. F., ApJ, in press
- Goldsmith P. F., Melnick G. J., Bergin E. A., et al. 2000, ApJ, 539, L123
- Graedel T. E., Langer W. D., Frerking M. A. 1982, ApJS, 48, 321
- Guélin M., Langer W. D., Wilson R. W. 1982, A&A, 107, 107
- Hasegawa T. I., Herbst E. 1993, MNRAS, 261, 83
- Hasegawa T. I., Herbst E., Leung C. M. 1992, ApJS, 82, 167
- Herbst E., Leung C. M. 1989, ApJS, 69, 271
- Katz N., Furman I., Biham O., Pirronello V., Vidali G. 1999, ApJ, 522, 305
- Kramer C. 1994, Spectral Line Calibration at the IRAM 30m Radiotelescope, IRAM Report.

- Krügel E., Walmsley C.M. A&A 130,5
- Lacy J. H., Knacke R., Geballe T. R., Tokunaga A. T. 1994, ApJ, 428, L69
- Lee H.-H., Bettens R. P. A., Herbst H. 1996, A&AS, 119, 111
- Léger A., Jura M., Omont A. 1985, A&A, 144, 147
- Linsky J. L., Diplas A., Wood B. E., Brown A., Ayres T. R., Savage B. D. 1995, ApJ, 451, 335
- Mathis J. S., Rumpl W., Nordsieck K. H. 1977, ApJ, 217, 425
- McKee C. F. 1989, ApJ, 345, 782
- Meyer D. M., Cardelli J. A., Sofia U. J. 1997, ApJ, 490, L103
- Monteiro T. S. 1985, MNRAS, 214, 419
- Myers P. C., Linke R. A., Benson P. J. 1983, ApJ, 264, 517
- Penzias A. A. 1981, ApJ, 249, 518
- Prasad S. S., Huntress W. T. 1982, ApJ, 260, 590
- Rogers S.D & Charnley S.B. 2001 ApJ, in press
- Roberts H., Millar T. J. 2000, A&A, 361, 388
- Roueff E., Tiné S., Coudert L.H., Pineau des Forêts G., Falgarone E., Gerin M. 2000, A&A , 354, L63
- Ruffle D. P., Hartquist T. W., Taylor S. D., Williams D. A. 1997, MNRAS, 291, 235
- Sadlej J., Rowland B., Devlin J. P., Buch V. 1995, J. Chem. Phys., 102, 4804
- Shu F. H., Adams F. C., Lizano S. 1987, ARA&A, 25, 23
- Smith D., Adams N. G. 1984, ApJ, 284, L13
- Spitzer L. 1978, Physical Processes in the Interstellar Medium (New York: Wiley)
- Tafalla M., Mardones D., Myers P. C., Caselli P., Bachiller R., Benson P. J. 1998, ApJ, 504, 900
- Tafalla M., Myers P. C., Caselli P., Walmsley C. M., in preparation
- Takahashi J., Williams D. A. 2000, MNRAS, 314, 273
- Tiné S., Roueff E., Falgarone E., Gerin M., Pineau des Forêts G., 2000, A&A, 356, 1039
- Umebayashi T., Nakano T. 1990, MNRAS, 243, 103

- Ungerechts H., Walmsley C. M., Winnewisser G. 1982, A&A, 111, 339
- Vandenbussche B., Ehrenfreund P., Boogert A. C. A., et al. 1999, A&A, 346, L57
- Viti S., Roueff E., Hartquist T. W., Pineau des Forets G., Williams D. A. 2001, A&A, 370, 557
- Walmsley C.M. 1987 p161 in "Physical Processes in Interstellar Clouds" (edited Morfill G.E., Scholer M.), NATO ASI Series C, Vol 210, publ. D.Reidel
- Ward–Thompson D., Motte F., André P. 1999, MNRAS, 305, 143 (WMA)
- Willacy K., Millar T. J. 1998, MNRAS, 298, 562
- Williams J.P., Bergin E.A., Caselli P., Myers P.C., Plume R. 1998, ApJ, 503, 689
- Williams J.P., Myers P.C., Wilner D.J., Di Francesco J. 1999 ApJ, 513, L61
- Wilson T.L., Rood R.T 1994, ARA&A, 32, 191
- Zucconi A., Walmsley C.M., Galli D. 2001, A&A, in press
- Wootten A., Snell R., Glassgold A. E. 1979, ApJ, 234, 876

Table 1: Molecular parameters used to calculate N_{TOT}

Transition	B MHz	μ Debye	Δv_{res} km s ⁻¹	N_{ch}
N ₂ D ⁺ (2–1)	38554.719	3.4	0.038	275
HC ¹⁸ O ⁺ (1–0)	42581.21	3.9	0.034	17
H ¹³ CO ⁺ (1–0)	43377.32	3.9	0.034	25
HC ¹⁷ O ⁺ (1–0)	43528.933	3.9	0.067	6
N ₂ H ⁺ (1–0)	46586.867	3.4	0.063	75
C ¹⁸ O(1–0)	54891.420	0.11	0.027	33
C ¹⁷ O(1–0)	56179.990	0.11	0.026	72
D ¹³ CO ⁺ (2–1)	35366.712	3.9	0.041	14
DCO ⁺ (2–1)	36019.76	3.9	0.041	22
DCO ⁺ (3–2)	36019.76	3.9	0.054	13

Table 2. Parameters of the “best fit” models

Parameters	Standard	Model 1	Model 2	Model 3	Model 4
Density Dist.	WMA	WMA	BAP	WMA	BAP
$\zeta(\text{s}^{-1})$	1.3×10^{-17}	5.0×10^{-19}	1.3×10^{-18}	6.0×10^{-18}	5.0×10^{-18}
$E_{\text{D}}(\text{CO})[\text{K}]$	1210	960	1210	1210	1210
$E_{\text{D}}(\text{N}_2)[\text{K}]$	787	600	600	787	787
$E_{\text{D}}(\text{O})[\text{K}]$	600	600
$a_{\text{min}}(\text{cm})$	1×10^{-6}	2.5×10^{-5}	1.0×10^{-5}	5.0×10^{-6}	1.0×10^{-6}
S	1.0	0.1	0.1	1.0	0.1
χ^2	...	4.7	6.7	1.6	5.4

Fig. 1.— Logarithmic values of the H_2 number density, $n(\text{H}_2)$, superposed upon the half maximum contours of the $\text{DCO}^+(2-1)$ (thin curve), the $\text{DCO}^+(3-2)$ (dashed curve) integrated intensity maps, and the 1.3mm continuum dust emission (dotted curve) convolved to a $22''$ beam (circle in the bottom right). The grey scale shows the $\text{DCO}^+(3-2)$ integrated intensity map (levels 50, 70, and 90% of the peak, 0.84 K km s^{-1} at offset $[20, -20]$). The density values in the figures are based on statistical equilibrium calculations (see text).

Fig. 2.— Map of the depletion factor f_{D} (grey scale) superposed to the 1.3mm continuum dust emission map of WMA, smoothed at a resolution of $22''$ (dotted contours). f_{D} ranges between 1 (at the core edges) and 10.8 (at offset $[24, -34]$); the grey scale (from light to dark) shows parts in the core with $f_{\text{D}} = 1, 3, 5, 7,$ and 9 . Dotted contours levels represent 30, 50, 70, and 90% of the 1.3mm map peak ($225 \text{ mJy}/22''$ at offset $[26, -21]$). The distance between the two peaks is about half a beam.

Fig. 3.— (*top left*) DCO^+ column density map; contour levels are between 30 and 90%, in steps of 20% of the map peak ($= 4.0 \times 10^{12} \text{ cm}^{-2}$, at $[20, -20]$). (*center left*) HCO^+ column density map; contour levels are as in the previous panel and the map peak is at offset $(0, 0)$ ($1.1 \times 10^{14} \text{ cm}^{-2}$). (*bottom left*) $N(\text{DCO}^+)/N(\text{HCO}^+)$ column density ratio map. Contour levels are 10, 30, and 50% of the map peak (0.06 ± 0.02 at offsets $[20, 20]$ and $[40, -20]$). The difference between the four positions inside the 50% contour level is not significant, taking into account the associated errors. (*top right*) N_2D^+ column density map (contours range between 30 and 90%, in steps of 20%, of the map peak ($= 4.4 \times 10^{12} \text{ cm}^{-2}$, at $[20, -20]$). (*center right*) N_2H^+ column density map; contour levels are as in the previous panel and the map peak is at offset $(20, -10)$ ($2.0 \times 10^{13} \text{ cm}^{-2}$). (*bottom right*) $N(\text{N}_2\text{D}^+)/N(\text{N}_2\text{H}^+)$ column density ratio map; contour levels are 10, 30, 50, 70% of the peak (0.26 at $[40, -20]$).

Fig. 4.— Dependence on radius of the depletion factor for CO (f_{D}) and N_2 (top panels), electron fraction and various ionic species (bottom panels) for the “standard model” (see Tab. 2 for input parameters) using the density distribution found by WMA (left panels) and BAP (right panels).

Fig. 5.— Column density (filled circles) versus impact parameter for (from top to bottom): CO, HCO^+ , DCO^+ , N_2H^+ , and N_2D^+ . White symbols are average column densities inside the corresponding bin, with the only exception of the value at $b = 0$ (see text).

Fig. 6.— Column density profiles predicted by the “best fit” models (solid curves) and deduced from observations (dotted curves). Left panels refer to models with a volume density profile from WMA (Model 1), whereas models shown in right panels assume the L1544 density profile from BAP (Model 2).

Fig. 7.— Column density profiles predicted by the “best fit” models with atomic oxygen (solid curves) and observed (dotted curves). As in Fig. 6, left panels refer to models with volume density profile from WMA (Model 3), whereas right panels show models with density profiles from BAP

(Model 4). The inclusion of atomic oxygen in the gas phase furnishes a better agreement with observed molecular ion column densities at the dust peak and with observed column density profiles.

Fig. 8.— Radial profiles of fractional abundances of electrons, HCO^+ , DCO^+ , N_2H^+ , and N_2D^+ predicted by Model 1 (top) and 3 (bottom; see Tab. 2). Dashed curves represent the depletion factor. Electron fractions are about one order of magnitude lower than deduced from “standard” chemical models without depletion. This affects the dynamical evolution of prestellar cores by shortening the ambipolar diffusion time scale.

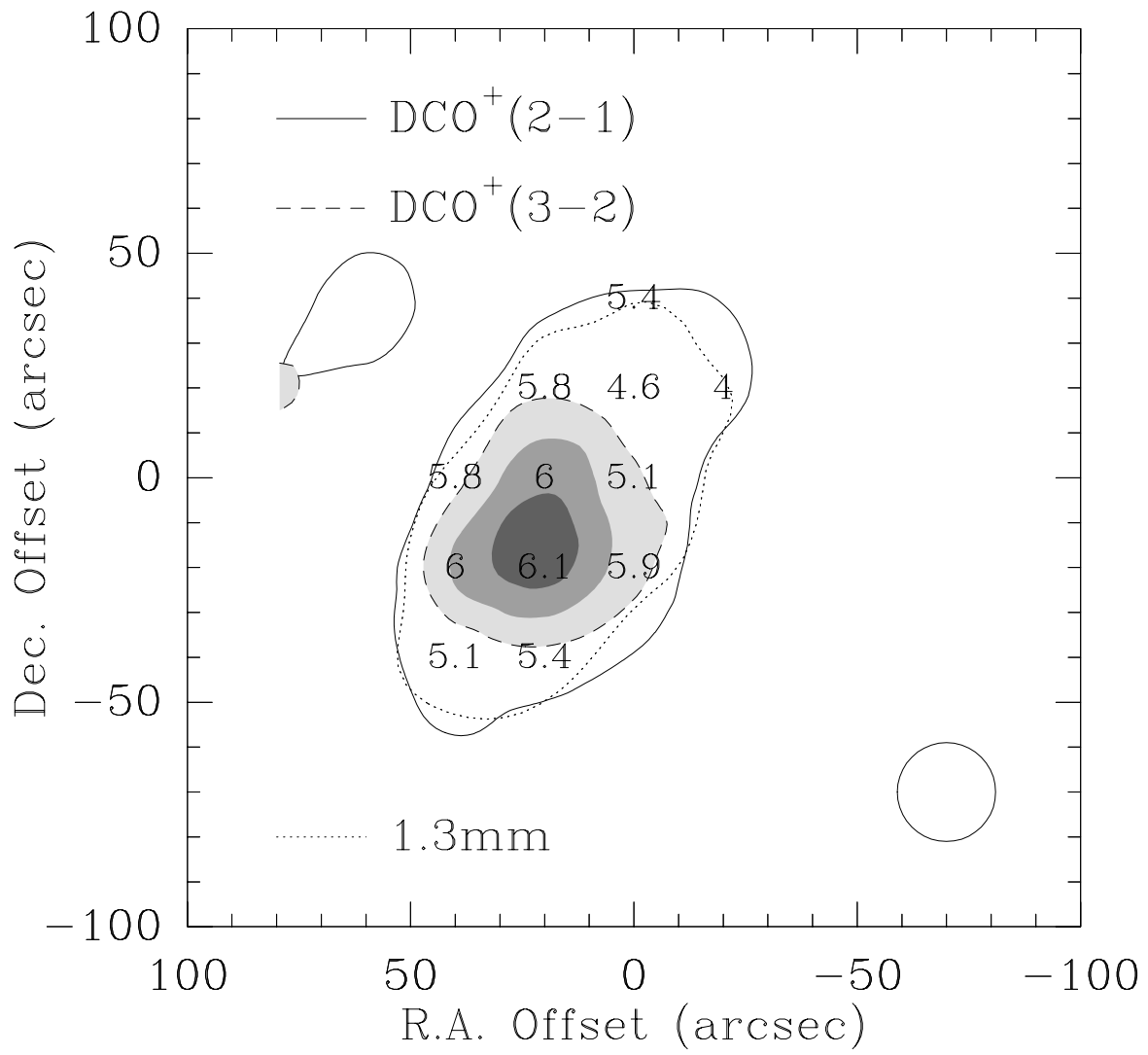


Fig.1

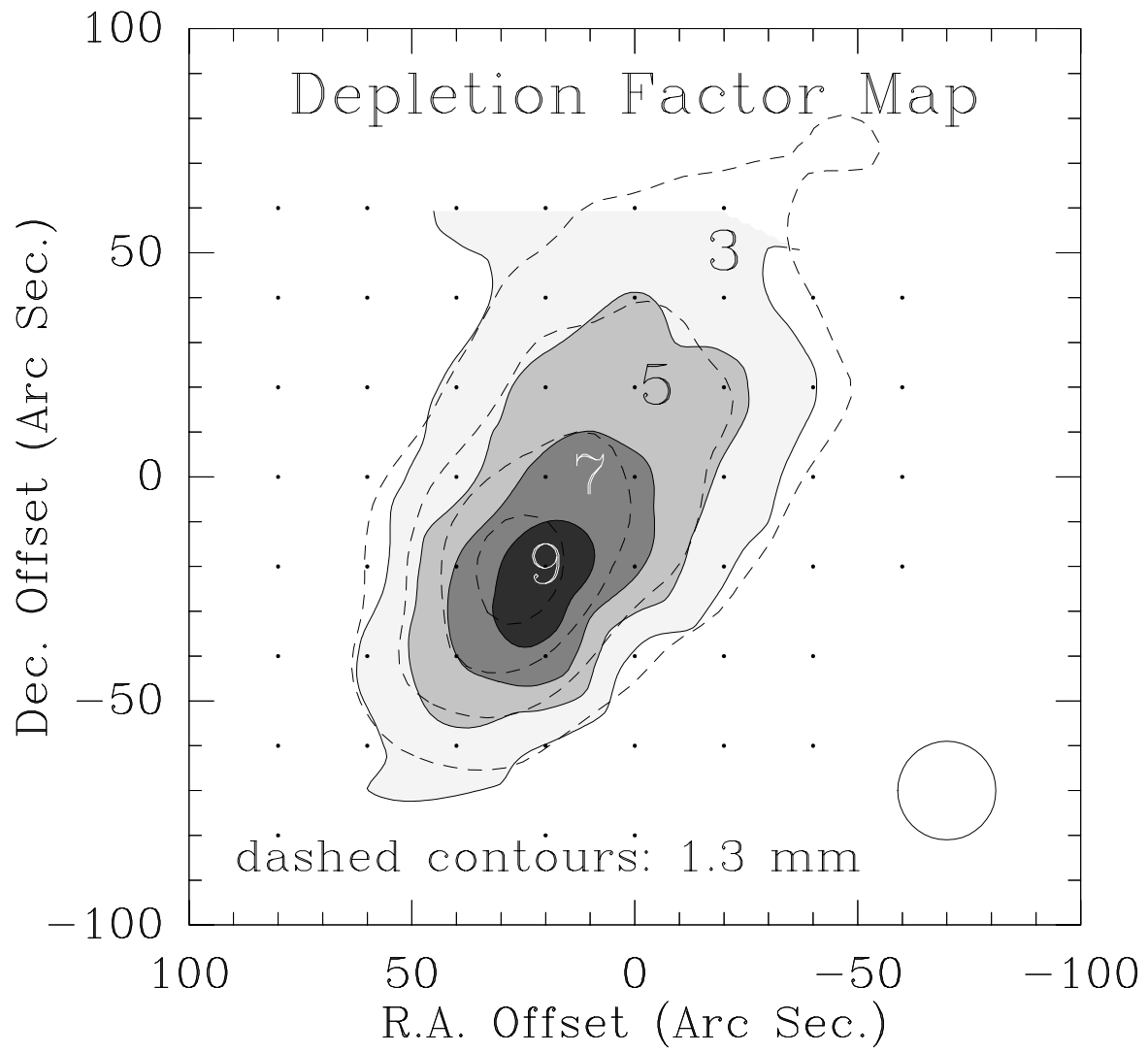


Fig.2

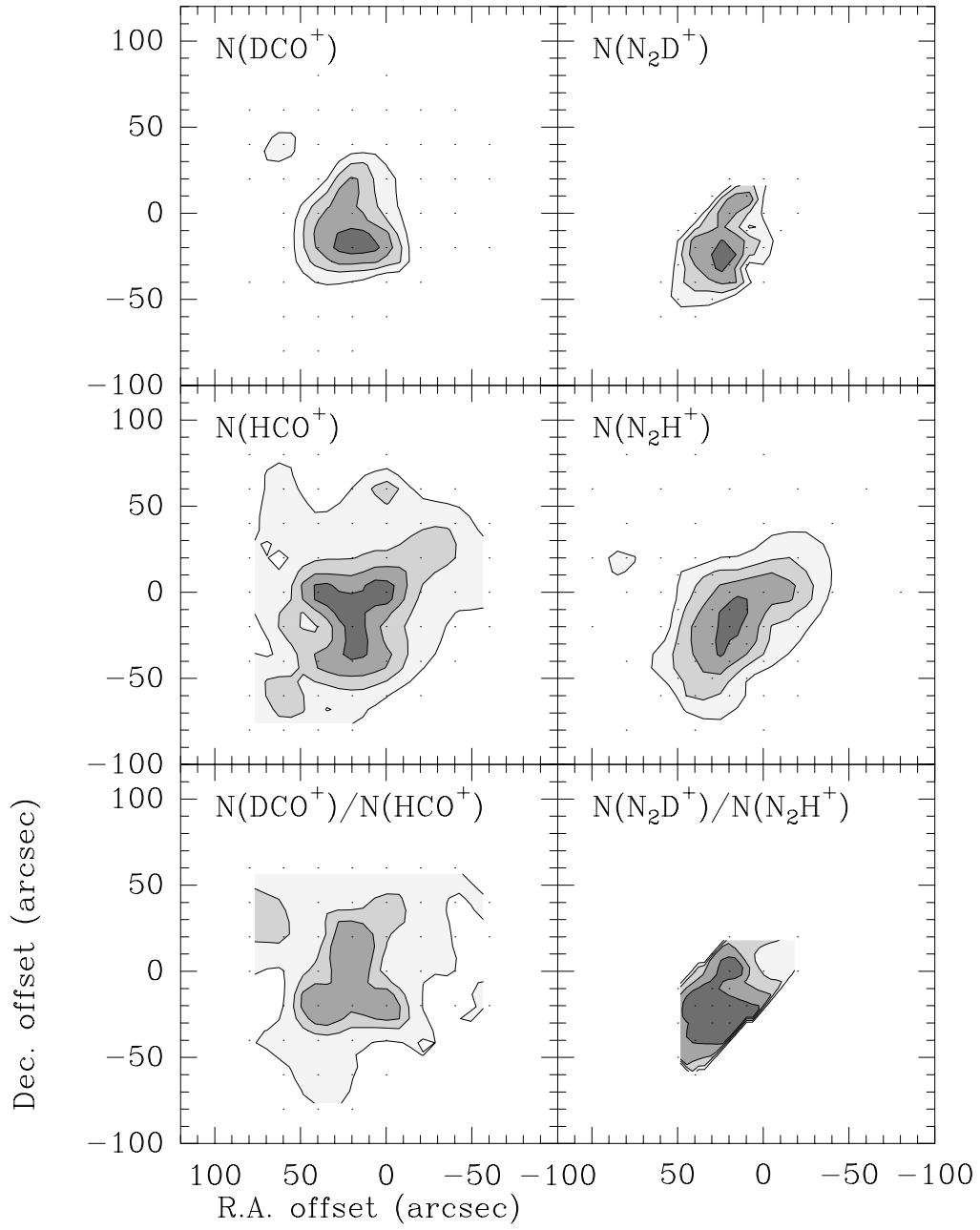


Fig.3

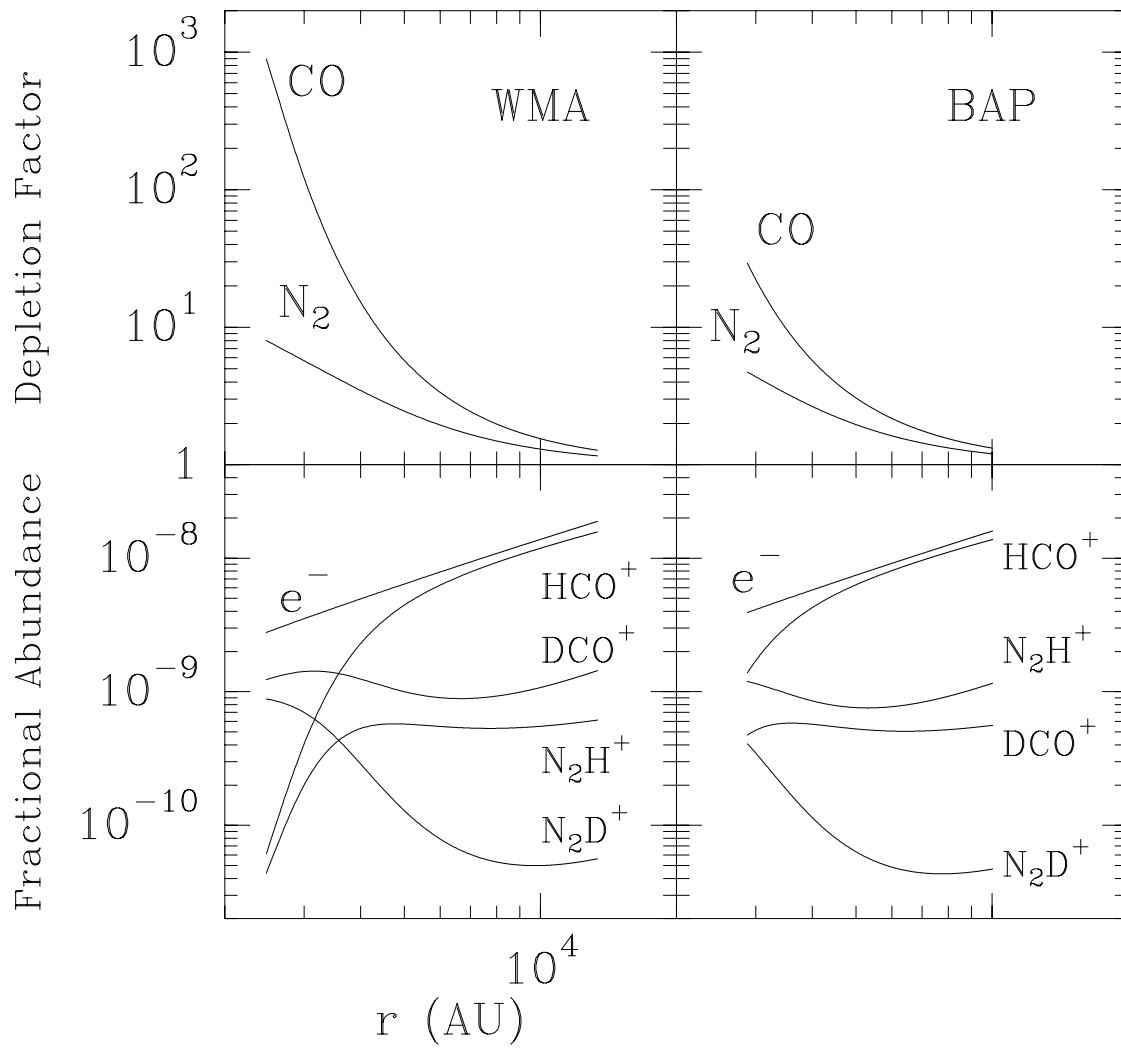


Fig.4

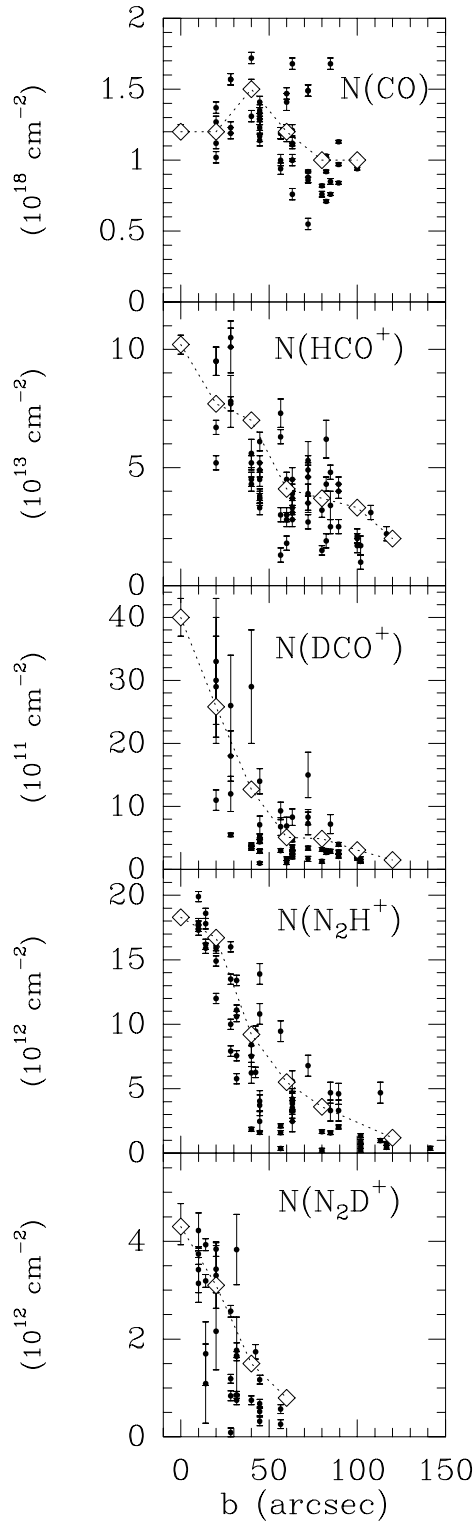


Fig.5

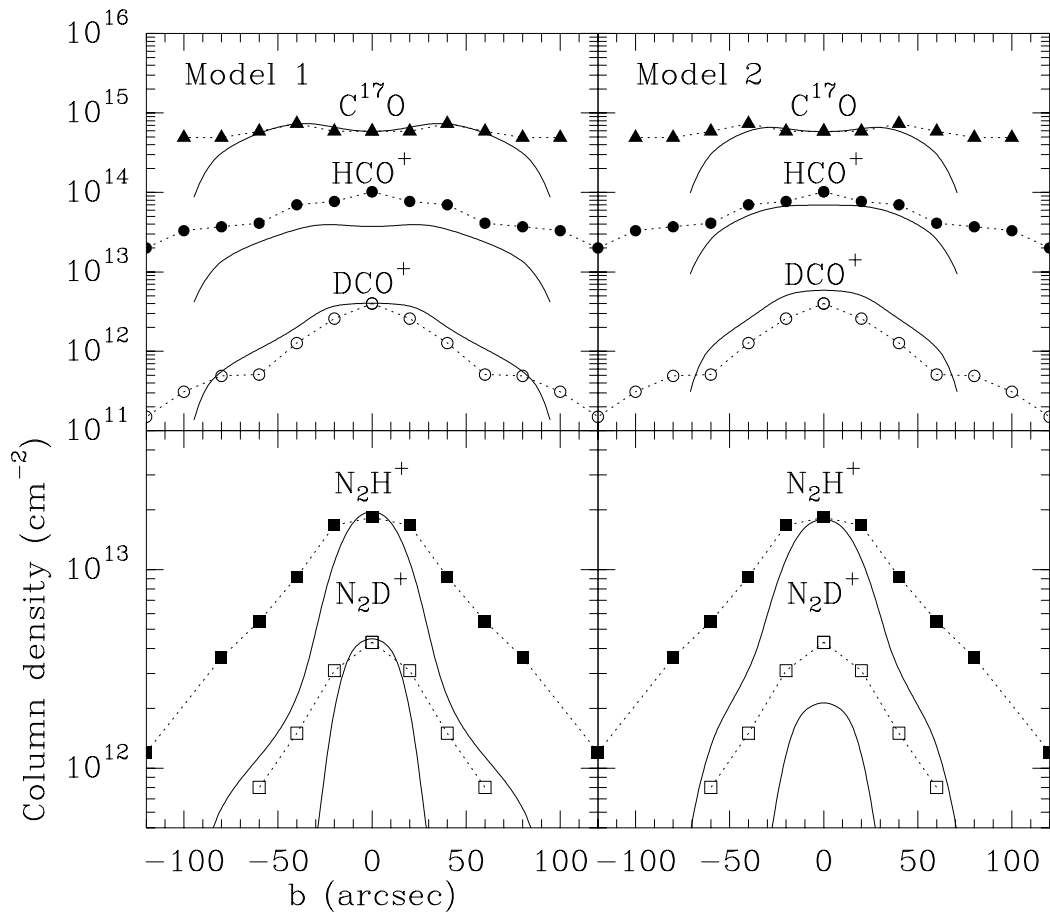


Fig.6

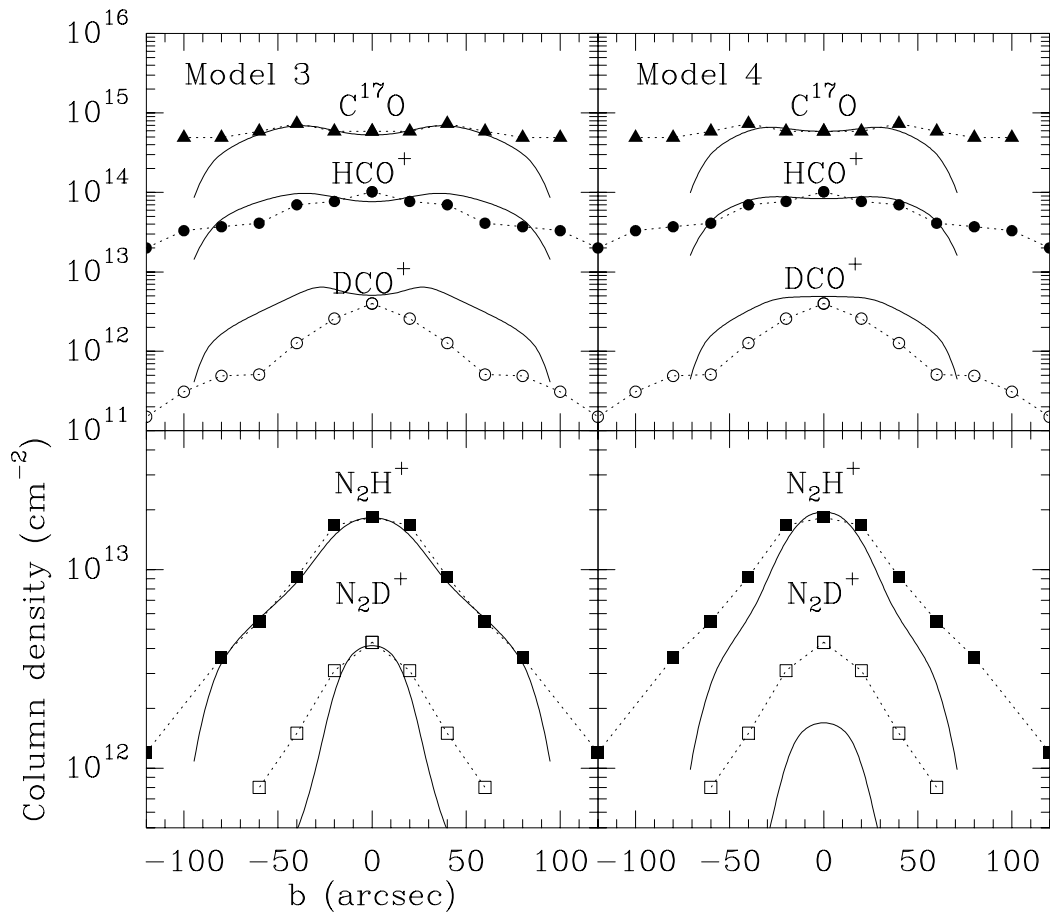


Fig.7

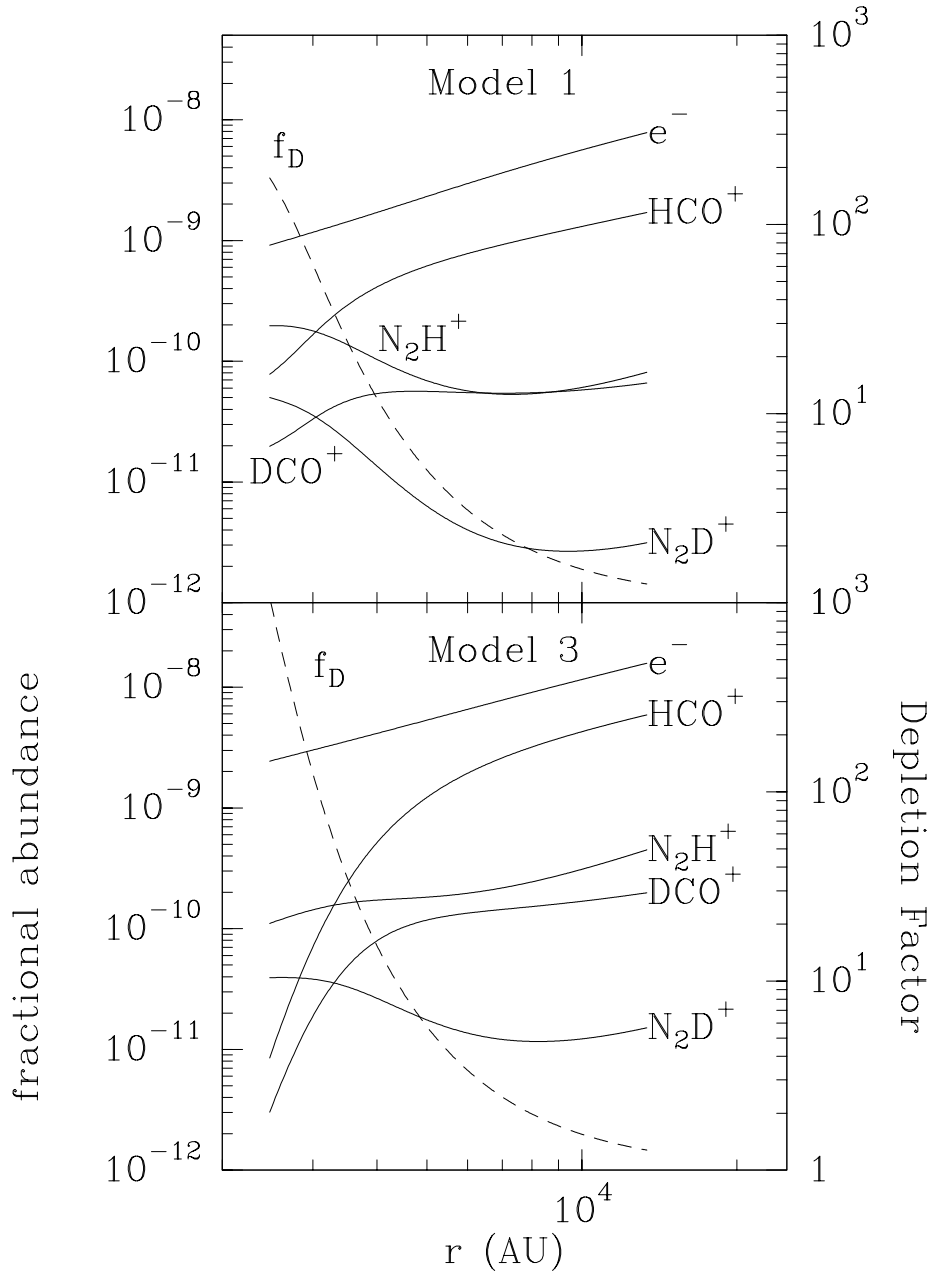


Fig.8